New insights into the formation and emplacement of impact melt rocks within the Chicxulub impact structure, following the 2016 IODP-ICDP Expedition 364

de Graaff, Sietze J.; Kaskes, Pim; Déhais, Thomas; Goderis, Steven; Debaille, Vinciane; Ross, Catherine H.; Gulick, Sean P.S.; Feignon, Jean Guillaume; Ferrière, Ludovic; Koeberl, Christian; Smit, Jan; Mattielli, Nadine; Claeys, Philippe

Link to publication in VU Research Portal

New insights into the formation and emplacement of impact melt rocks within the Chicxulub impact structure, following the 2016 IODP-ICDP Expedition 364

Sietze J. de Graaff[1,2,†], Pim Kaskes[1,2,†], Thomas Déhais[1,2,†], Steven Goderis[1,†], Vinciane Debaille[2,†], Catherine H. Ross[3,†], Sean P.S. Gulick[3,4,†], Jean-Guillaume Feignon[5,†], Ludovic Ferrière[6,†], Christian Koeberl[5,†], Jan Smit[7,†], Nadine Mattielli[2,†], and Philippe Claeys[1,†]

[1]*Analytical, Environmental & Geo-Chemistry Research Unit, Department of Chemistry, Vrije Universiteit Brussel, AMGC-WE-VUB, Pleinlaan 2, 1050 Brussels, Belgium*
[2]*Laboratoire G-Time, Université Libre de Bruxelles, ULB, Avenue F.D. Roosevelt 50, 1050 Brussels, Belgium*
[3]*Institute for Geophysics & Department of Geological Sciences, Jackson School of Geosciences, University of Texas at Austin, Austin, Texas 78758, USA*
[4]*Center for Planetary Systems Habitability, University of Texas at Austin, Austin, Texas 78712, USA*
[5]*Department of Lithospheric Research, University of Vienna, Althanstrasse 14, A-1090 Vienna, Austria*
[6]*Natural History Museum, Burgring 7, A-1010 Vienna, Austria*
[7]*Department of Earth Sciences, Vrije Universiteit Amsterdam, De Boelelaan 1085, 1081 HV Amsterdam, Netherlands*

ABSTRACT

This study presents petrographic and geochemical characterization of 46 pre-impact rocks and 32 impactites containing and/or representing impact melt rock from the peak ring of the Chicxulub impact structure (Yucatán, Mexico). The aims were both to investigate the components that potentially contributed to the impact melt (i.e., the pre-impact lithologies) and to better elucidate impact melt rock emplacement at Chicxulub. The impactites presented here are subdivided into two sample groups: the lower impact melt rock–bearing unit, which intrudes the peak ring at different intervals, and the upper impact melt rock unit, which overlies the peak ring. The geochemical characterization of five identified pre-impact lithologies (i.e., granitoid, dolerite, dacite, felsite, and limestone) was able to constrain the bulk geochemical composition of both impactite units. These pre-impact lithologies thus likely represent the main constituent lithologies that were involved in the formation of impact melt rock. In general, the composition of both impactite units can be explained by mixing of the primarily felsic and mafic lithologies, but with varying degrees of carbonate dilution. It is assumed that the two units were initially part of the same impact-produced melt, but discrete processes separated them during crater formation. The lower impact melt rock–bearing unit is interpreted to represent impact melt rock injected into the crystalline basement during the compression/excavation stage of cratering. These impact melt rock layers acted as delamination surfaces within the crystalline basement, accommodating its displacement during peak ring formation. This movement strongly comminuted the impact melt rock layers present in the peak ring structure. The composition of the upper impact melt rock unit was contingent on the entrainment of carbonate components and is interpreted to have stayed at the surface during crater development. Its formation was not finalized until the modification stage, when carbonate material would have reentered the crater.

INTRODUCTION

Chicxulub Impact Structure

The ~200-km-diameter Chicxulub impact structure, located on the Yucatán Peninsula, Mexico, represents one of the best-preserved large complex impact structures on Earth (Fig. 1; Hildebrand et al., 1991; Gulick et al., 2008). It is the only known terrestrial impact structure preserving a topographic peak ring (Morgan et al., 1997, 2016), and it is linked to the extinction of the nonavian dinosaurs (e.g., Swisher et al., 1992; Smit, 1999; Schulte et al., 2010). The structure formed at $66.038 \pm 0.025/0.049$ Ma (Renne et al., 2013) by the impact of an ~12-km-diameter body with a composition similar to that of a carbonaceous chondrite (e.g., Shukolyukov and Lugmair, 1998; Quitté et al., 2007; Goderis et al., 2013; Collins et al., 2020) on an ~3-km-thick Mesozoic carbonate and evaporite platform overlying crystalline basement rock (Morgan et al., 2016).

At present, the impact structure is covered by ~1 km of Cenozoic sediments, significantly inhibiting the direct study of the impact structure and lithologies formed as a consequence of the impact (commonly referred to as impactites). Consequently, current understanding of the Yucatán basement, the Chicxulub impact structure, and its impactite suite is mostly based on ejecta material (e.g., Koeberl and Sigurdsson, 1992; Koeberl, 1993; Belza et al., 2015) and samples recovered from petroleum exploration and scientific drilling campaigns (e.g., Lopez Ramos, 1975; Hildebrand et al., 1991; Swisher et al., 1992; Urrutia-Fucugauchi et al., 1996; Claeys et al., 2003; Tuchscherer et al., 2004a; and references therein). The drilling campaigns

Sietze de Graaff https://orcid.org/0000-0003-0865-997X

[†]sietze.de.graaff@vub.be; pim.kaskes@vub.be; thomas.dehais@vub.be; steven.goderis@vub.be; vinciane.debaille@ulb.ac.be; catherine.ross@utexas.edu; sean@ig.utexas.edu; jean-guillaume.feignon@univie.ac.at; ludovic.ferriere@nhm-wien.ac.at; christian.koeberl@univie.ac.at; j.smit@vu.nl; nadine.mattielli@ulb.ac.be; phclaeys@vub.be.
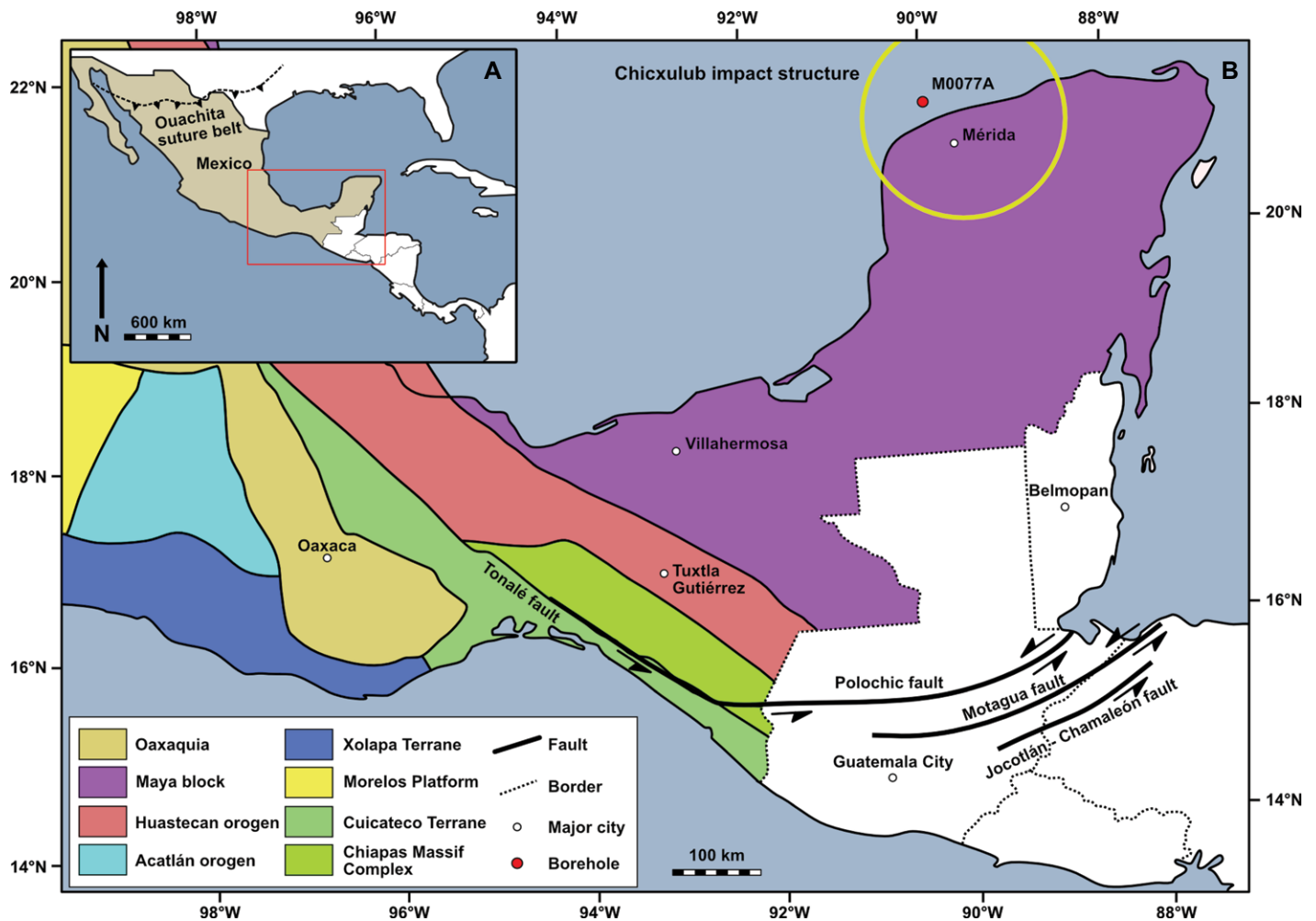
Figure 1. (A) Map overview of the Mexico region and the Yucatán Peninsula. (B) Tectonostratigraphic map of southeastern Mexico using the proposed subdivision of tectonostratigraphic domains suggested by Ortega-Gutiérrez et al. (2018). Figure is modified from Ortega-Gutiérrez et al. (2018) and Weber et al. (2012, 2018).

within the impact structure have sampled impact (melt-bearing) breccias (suevite) and impact melt rocks in the Petróleos Méxicanos (PEMEX) Chicxulub-1 (C-1) and Yucatán-6 (Y-6) drill cores (Hildebrand et al., 1991; Kring and Boynton, 1992; Swisher et al., 1992; Koeberl, 1993; Schuraytz et al., 1994; Ward et al., 1995; Claeys et al., 2003; Kettrup and Deutsch, 2003) and in the International Continental Scientific Drilling Program (ICDP) Yaxcopoil-1 (Yax-1) drill core (Tuchscherer et al., 2004a, 2004b, 2005, 2006). Cretaceous target rock affected by the impact at the crater rim was exclusively recovered in the Yax-1 drill core (e.g., Wittmann et al., 2004; Belza et al., 2012) and as clasts in breccia units in the other drillings. Importantly, none of these drill cores penetrated into the underlying basement, and knowledge of the Yucatán crystalline basement was therefore, until recently, solely based on the study of crystalline clasts in impact breccias (e.g., Kettrup and Deutsch, 2003).

In 2016, International Ocean Discovery Program (IODP) and ICDP Expedition 364 drilled the peak ring of the Chicxulub impact structure, recovering a near-continuous core from 505.7 m below seafloor (mbsf) down to 1334.69 mbsf at Hole M0077A (Morgan et al., 2017). This core is the first direct sampling of largely uninterrupted crystalline basement and impact melt rocks (Morgan et al., 2016, 2017) from the Chicxulub impact structure. This study concerns the petrography and major- and trace-element composition of 46 pre-impact rocks and 32 impactites containing and/or representing impact melt rock from IODP-ICDP Hole M0077A. Through the study of both the impactites and its precursor material, the pre-impact lithologies, we aimed to better understand impact melt formation and emplacement at the Chicxulub impact structure. Moreover, this study expands upon the limited availability of petrographic and

geochemical data concerning the crystalline basement of the Yucatán Peninsula.

Geological Setting

At the site of the Chicxulub impact structure, the subsurface geology of the Yucatán Peninsula mainly consists of structurally simple, nearly horizontal strata of Lower Cretaceous to Quaternary carbonates and evaporites (Lopez Ramos, 1975; Hildebrand et al., 1991) overlying crystalline basement rock yielding ages ranging from Pan-African (ca. 546 Ma; Krogh et al., 1993; Kamo and Krogh, 1995, 2011; Keppie et al., 2011) to Carboniferous (326 ± 5 Ma; Rasmussen et al., 2019; Zhao et al., 2020; Ross et al., 2021). Here, the crystalline basement is part of the Maya block, the southeasternmost Mexican geological terrane (Fig. 1; Keppie et al., 2011; Weber et al., 2012, 2018). The Maya block has traditionally been inferred to encompass the

Yucatán Peninsula in the north, including the coastal plains of the western and northern Gulf of Mexico (Weber et al., 2012) to the Chiapas Massif Complex in the south (Fig. 1B; Keppie et al., 2011; Weber et al., 2012, 2018), with the northern and northeastern boundaries bordered by continental shelves and oceanic lithosphere (Alaniz-Álvarez et al., 1996; Keppie et al., 2011).

The exact extent of the Maya block remains open to discussion. Originally, the Maya block was thought to be bordered by the Grenvillian-aged Oaxaquia block (in the NW) and the roughly E-W–trending Polochic, Motagua, and Jocotlán-Chamaleón fault systems (in the S), which separated the Maya block from the Caribbean plate (Fig. 1; Dengo, 1969; Donnelly et al., 1990; Weber et al., 2012, 2018). However, recent work by Ortéga-Gutiérrez et al. (2018) suggests that the Chiapas Massif Complex is a distinct tectonostratigraphic domain, separated from the Maya block by the Huastecan Paleozoic orogenic belt (Fig. 1B). This mostly buried orogenic system extends northwestward until the Ouachita suture belt (Fig. 1A) and separates the Oaxaquia and Cuicateco terranes in the west from the Maya block in the north and east (Fig. 1B). Paleomagnetic reconstruction indicates that the Maya block behaved as a single cohesive unit since the Late Triassic (ca. 230 Ma) and that during the breakup of Pangea, this block rifted away from the southern margin of Laurentia to open the Gulf of Mexico between 230 and 150 Ma (Steiner, 2005). The Maya block reached its present paleolatitude relative to North America during the Late Jurassic (ca. 150 Ma; Molina-Garza et al., 1992), after which it remained geologically stable until the Chicxulub impact event (66 Ma; Renne et al., 2013). This geological stability allowed for the formation of an ~3-km-thick carbonate platform of limestone, dolomite, marl, and anhydrite on top of the basement (Lopez Ramos, 1975; Kring, 2005). At the time of the impact, the platform was a carbonate ramp that deepened to the N and NE with water depths ranging from ~100 to 2000 m, with an average depth of ~600 m (Gulick et al., 2008).

During the impact event, the carbonates and evaporites overlying the basement within the area of the transient cavity were either ejected from the crater or incorporated into gravity flows during crater modification (Gulick et al., 2019). The sedimentary units are preserved within the ring structures, comprise kilometer-scale slump blocks within the crater's terrace zone, and appear as clasts in the Chicxulub suevite (Claeys et al., 2003; Belza et al., 2012). This breccia also preserves clasts of mica schist, quartz gneiss, metasediments, granitic rock, and dolerite from the crystalline basement (Claeys et al., 2003;

Kettrup and Deutsch, 2003; Tuchscherer et al., 2005; Morgan et al., 2017). So far, none of these diverse lithologies have been successfully linked to similar lithologies cropping out at the surface of the Maya block or in any other tectonostratigraphic domain (Fig. 1B).

IODP-ICDP Expedition 364

IODP-ICDP Expedition 364 Hole M0077A (Fig. 1; hereafter Hole M0077A) sampled the peak ring of the Chicxulub impact structure, recovering a total of 303 continuous subcores and associated downhole logs, with a total cored length of 828.99 m sampling a maximum depth of 1334.69 mbsf (Fig. 2; Morgan et al., 2017). The drill core was subdivided into four distinct units (Morgan et al., 2017).

Unit 1 comprises postimpact, sedimentary Cenozoic crater infill from 505.70 to 617.33 mbsf and is further subdivided into seven lithostratigraphic subunits based on changes in lithologies and specific surfaces indicating erosional truncation of underlying facies (Morgan et al., 2017). It is not further discussed in this study.

Unit 2, from 617.33 to 721.61 mbsf, comprises an impact melt–bearing polymict breccia with a particulate matrix that is, therefore, referred to as suevite (following Stöffler and Grieve, 2007; Gulick et al., 2017a). The suevite unit is subdivided into three subunits based on sedimentary features and matrix or groundmass characteristics (Fig. 2; Gulick et al., 2017a); see Gulick et al. (2019) for analysis and discussion of the depositional processes for Unit 2.

Unit 3 consists of CaO-rich green schlieren and SiO$_2$-rich impact melt rock from 721.61 to 747.02 mbsf. The first occurrence of massive black impact melt rock defines the upper boundary of this unit, yet this boundary is gradual, transitioning from coarse-grained, poorly sorted suevite to impact melt rock. The lower boundary is set at the first occurrence of intersected granitoid exceeding 1 m in length (Gulick et al., 2017a), although impact melt rock bodies are observed down to 759.02 mbsf, ~12 m below the set boundary. Unit 3 is further subdivided into two subunits based on the occurrence of green schlieren. The top unit between 721.61 and 737.56 mbsf contains black impact melt rock and green schlieren, both recognizable at the macroscopic and microscopic scale (Fig. 2). The lower unit, between 737.56 and 747.02 mbsf, is composed of black impact melt rock containing crystalline basement clasts (Fig. 2; Gulick et al., 2017a).

Unit 4, from 747.02 to 1334.69 mbsf, is primarily composed of felsic crystalline basement rock of granitoid material that is petrographically characterized as coarse-grained granite to

syenite, which hosts aplite and pegmatite dikes (Gulick et al., 2017b). This unit is pervasively intruded by pre-impact magmatic dikes (varying from igneous dolerite to felsite, and dacite) and dikes of impact melt rock and impact melt rock–bearing breccia (similar to suevite; Gulick et al., 2017b). These dikes of impact melt rock and impact melt rock–bearing breccia are hereafter referred to as "impactite dikes." Most contacts between the impactite dikes and granitoid are not sharp, are generally heavily deformed, and occur at distinctly differing angles (Fig. 2). Interestingly, the impactite dikes are not observed to crosscut, or interact with, the pre-impact magmatic dikes present in the granitoid. The impactite dikes are most prevalent toward the bottom of the core between 1206.98 and 1334.69 mbsf. These observations notwithstanding, the granitoid is not further subdivided into subunits (Gulick et al., 2017b).

This study follows the same subdivision as described in Morgan et al. (2017) and refers to all lithologies present before the impact event as pre-impact lithologies (i.e., carbonate, crystalline basement, and other clasts in the suevite and impact melt rock), whereas lithologies that formed as a result of the impact are referred to as impactites. Furthermore, for additional clarity, we subdivided the impactite units presented in this study into two sample groups based on macroscopic lithostratigraphic variations and core depth: (1) the upper impact melt rock unit, equivalent to Unit 3, and (2) the lower impact melt rock–bearing unit, contained in Unit 4. The upper impact melt rock unit is exposed at a well-defined depth interval and has clear (albeit gradual) boundaries with the overlying suevite (Unit 2) and underlying basement rock (Unit 4). However, the extent of the lower impact melt rock–bearing unit is more varied, with impactite dikes exposed at different intervals along the lower portion of the Hole M0077A core (Fig. 2). Smaller impactite dikes (not larger than a couple of meters) are exposed at 917.17, 995.24, and 1063.52 mbsf, while the bulk of the lower impact melt rock–bearing unit is exposed between 1206.98 and 1334.69 mbsf, where impactite dikes are interspersed with large blocks of granitoid and other entrained crystalline pre-impact lithologies.

Importantly, because impact melt rock was emplaced rapidly after impact (Morgan et al., 2016; Riller et al., 2018), and crosscutting relations between each individual lower impact melt rock–bearing unit interval are not discernible within a single core, we consider here all impactite dikes exposed in Unit 4 as "lower impact melt rock–bearing unit." This lithostratigraphic subdivision aims to clearly subdivide the lithological units of Chicxulub presented here in
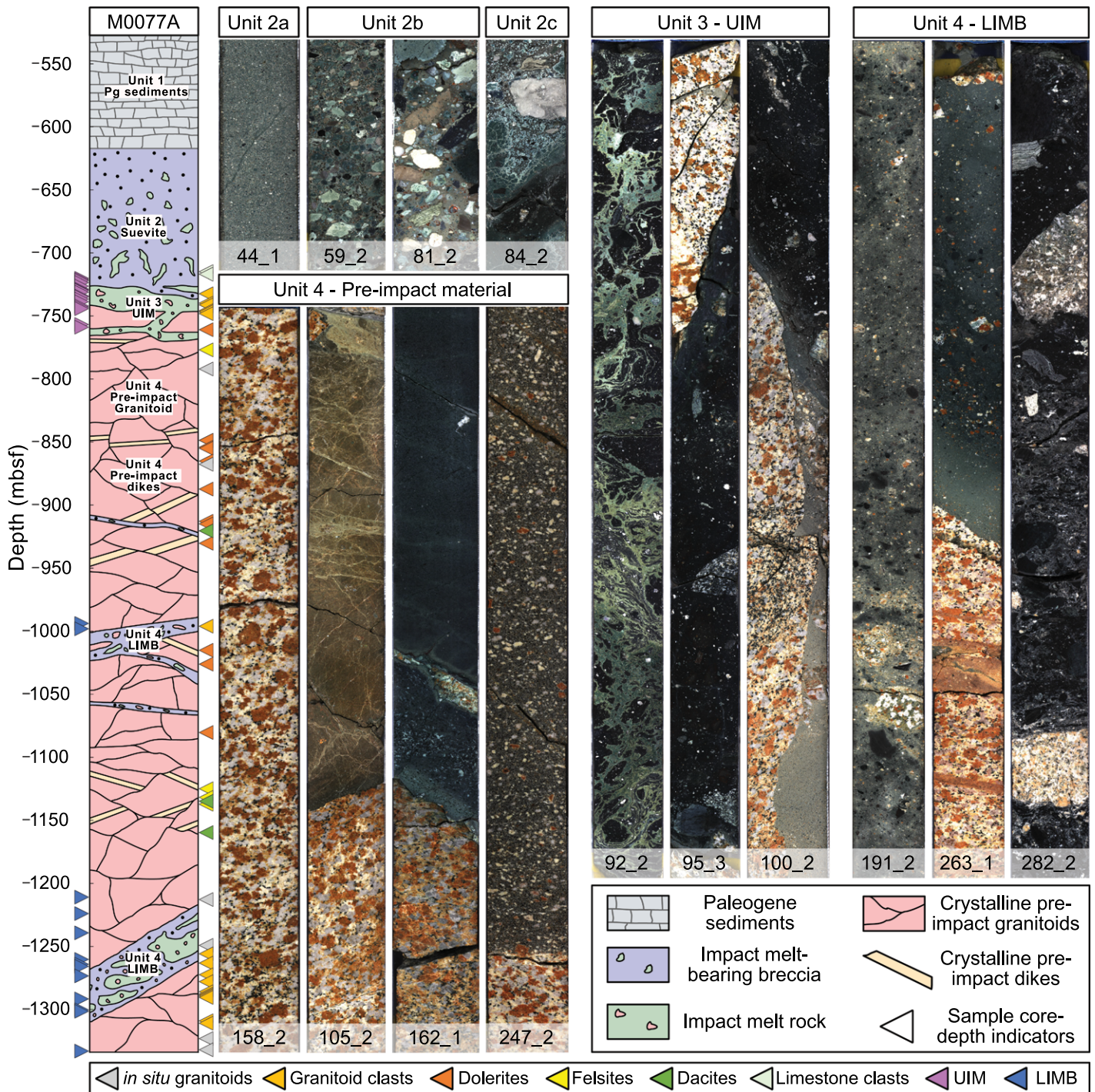
Figure 2. International Ocean Discovery Program (IODP) and International Continental Scientific Drilling Program (ICDP) Expedition 364 Hole M0077A schematic core overview (modified from Rae et al., 2019), with representative core sections of the units proposed in Morgan et al. (2017): Unit 2—showing the variation in the suevite unit with depth; Unit 3—showing the variation from green schlieren and black melt (notice the mingling textures) to black melt with clasts and black melt with basement interaction; Unit 4—lower impact melt rock–bearing unit, showing the variation from gray to black melt; Unit 4—pre-impact material, showing, from left to right, granitoid (158_2), felsite (105_2), dolerite (162_1), and dacite (247_2). Core width is consistently ~83 mm for each reported unit. Colored arrows indicate the sampling intervals of the different pre-impact (in situ granitoids: *n* = 6; granitoid clasts: *n* = 18; dolerites: *n* = 13; felsites: *n* = 4; dacites: *n* = 3; limestone clasts: *n* = 2) and impactite lithologies (upper impact melt rock unit: *n* = 19; lower impact melt rock–bearing unit: *n* = 13) presented in this study. See Appendix S1 for a detailed sample list (see text footnote 1). UIM—upper impact melt rock unit; LIMB—lower impact melt rock–bearing unit; mbsf—meters below seafloor.

order to better understand impact melt formation in the crater.

Significance of the Expedition 364 Drill Core

Prior to IODP-ICDP Expedition 364, the understanding of impact melt formation in the Chicxulub impact structure was mostly based on impact melt rocks and melt particles recovered from the PEMEX C-1 and Y-6 drill cores (Hildebrand et al., 1991; Kring and Boynton, 1992; Swisher et al., 1992; Koeberl, 1993; Schuraytz et al., 1994; Ward et al., 1995; Claeys et al., 2003; Kettrup and Deutsch, 2003), from Universidad Nacional Autónoma de México (UNAM) shallow wells 5 and 7 (Urrutia-Fucugauchi et al., 1996), and from the ICDP Yax-1 drill core (Kring et al., 2004; Stöffler et al., 2004; Tuchscherer et al., 2004a, 2004b, 2005, 2006; Wittmann et al., 2004).

Melt particles were also studied as proximal ejected material recovered all around the Gulf of Mexico (Koeberl and Sigurdsson, 1992; Koeberl, 1993; Belza et al., 2015). Based on these materials, the impact melt of the Chicxulub impact structure was inferred to have formed as the result of bimodal melting and mixing of felsic and mafic target rock components (e.g., Tuchscherer et al., 2004a, 2005, 2006), producing an intermediate andesitic composition with additional dilution by a carbonate component (Claeys et al., 2003; Tuchscherer et al., 2006).

Moreover, significant low-temperature seawater alteration affected the Chicxulub impact melt rock and impact melt particles (Ames et al., 2004; Hecht et al., 2004; Zürcher and Kring, 2004). The impact melt particles were shown to be heterogeneous both in major- and trace-element concentrations and isotopic compositions (e.g., Kettrup et al., 2000; Kettrup and Deutsch, 2003; Tuchscherer et al., 2006; Belza et al., 2015). These studies also identified and highlighted the complexities of the Yucatán basement by sampling and classifying a multitude of pre-impact lithologies not exposed at the surface, including metasediments, gneiss, granite, granodiorite, amphibolite, gabbro, and mica schist (e.g., Koeberl, 1993). Interestingly, the pre-impact lithologies sampled in these drilling campaigns were constituted predominantly of felsic crystalline basement clasts (granite and granodiorite; Tuchscherer et al., 2005) and sedimentary rocks (metasediments and carbonate; Koeberl, 1993). Mafic clasts that were identified, such as amphibolite, gabbro, and mica schist clasts (Kettrup and Deutsch, 2003; Tuchscherer et al., 2004b), were comparatively sparse, comprising $\ll 2.5$ vol% of the total clastic content (Tuchscherer et al., 2005, for Yax-1). This find-

ing is counterintuitive to the observation that the impact melt rock exhibits an andesitic composition, as the pervasive melting of felsic rocks would require a correspondingly large mafic contribution, but to date no ubiquitous mafic component has been identified.

Importantly, the aforementioned cores from which melt particles and impact melt rock were sampled did not extend deeper than the top of the impact melt rock layer (equivalent to Unit 3a in this study; Fig. 2) and therefore never sampled the contact between the impact melt units and underlying crystalline rocks. Intrinsically, previous studies had to discuss impact melt generation without having access to the crystalline basement section. Improved discussion is now possible through the large continuous basement samples recovered in Hole M0077A. The study of both impactite and pre-impact material extracted from Hole M0077A, thus, becomes a necessity to advance our understanding of impact melt formation associated with large impact events in general and the Chicxulub impact structure in particular.

METHODS

Sample Selection and Preparation

To obtain representative samples of pre-impact and impactite lithologies, two sampling campaigns of the Hole M0077A core were conducted in 2017 and 2018 to supplement the material obtained during the IODP sampling party in fall 2016. Samples of representative lithologies were selected based on a priori studies of core descriptions (Morgan et al., 2017) and macroscopic observations achieved on site. Special care was taken to sample each individual pre-impact and impactite lithology away from other lithological contacts to ensure that the entire geochemical range of Units 3 and 4 of the Hole M0077A core could be determined. Here, pre-impact lithologies included clasts and in situ (i.e., not as clasts in breccia or impact melt rock) igneous granitoid, and in situ dolerite, felsite, and dacite. Limestone samples were only recovered as clasts from the suevite.

Equigranular granitoid samples were taken both in situ at different intervals ($n = 6$) to assess variation with core depth, and as clasts in the impact melt rock ($n = 18$) to ascertain the potential effects of impact melt interaction and/or variation in clasts entrained in the impactite units. Where possible, equigranular fine-grained sections were preferred when sampling pre-impact magmatic dikes in order to avoid the effects of phenocryst accumulation, as this process could potentially bias the geochemical results. For the impactites, a wide variety of impact melt rock or

impact melt rock–bearing material was sampled throughout the core, but sampling focused on black, macroscopically homogeneous, clast-poor core sections. In total, 46 pre-impact rocks and 32 impactites were collected and prepared for geochemical and petrographic analyses. Specific core depths and the lithological context of these samples can be found in Appendix S1.[1]

Before crushing, samples showing alteration veins, weathered surfaces, and/or instances where different lithologies, other than the main sampling target, were present, were carefully removed using a diamond board table saw. The samples were subsequently washed with Milli-Q water in an ultrasonic bath before crushing. Homogenized powdered samples were produced at the Vrije Universiteit Brussel (VUB). Approximately 10 cm³ samples were crushed using an agate mortar and pestle before powdering using a Pulverisette-5 agate ball mill. Major- and trace-element analysis was subsequently carried out at the Laboratoire G-Time of the Université Libre de Bruxelles (ULB) in a Class 1000 clean laboratory. Complete digestion of homogenized powdered samples was achieved using alkaline fusion and subsequent dissolution in 2 M HNO$_3$. Approximately 50 mg of powder was mixed with a fluxing agent of 0.8 g of lithium metaborate (LiBO$_2$, 99.997%) and 0.2 g of lithium tetraborate (Li$_2$B$_4$O$_7$, 99.998%) and subsequently melted into a glass bead at 1000 °C for 10 min. After cooling, the glass bead was transferred to a 50 mL 2 M HNO$_3$ solution until fully digested at room temperature, while continuously being stirred with a magnetic impeller. Loss on ignition was determined on separate powders (0.5 g) in a muffle furnace at 1000 °C over the course of 1 h. Sample nomenclature used here signifies the Core#_Section#_Top(cm)_Bottom(cm) to show the exact interval sampled, where centimeter (cm) notation is the distance down the core section from the top.

Major-Element Abundance Measurements

For major-element content measurements, aliquots of digested sample solution were diluted with 5% HNO$_3$ and doped with Y as an internal standard for checking (and if necessary, correcting) instrumental drift. Solutions were measured on an iCAP 7000 Series inductively

---

[1]Supplemental Material. Appendix S1, containing all geochemical data and specific core depths of all samples and geochemical results for geologic reference materials presented in the article. Figures S1–S3, containing thinsection photographs of representative pre-impact lithologies. Please visit https://doi.org/10.1130/GSAB.S.14356214 to access the supplemental material, and contact editing@geosociety.org with any questions.

coupled plasma–optical emission spectrometer (ICP-OES) operated using the Qtegra software package. Oxide concentrations were determined by comparing interference-corrected spectrum intensities against a calibration curve of multistandard element solutions of Si, Mg, Fe, Al, Ca, Na, Ti, K, P, Mn, and Cr in a 5% HNO_3 solution with known concentration. These standard solutions were doped with an ultrapure metaborate/tetraborate solution to match the matrix resulting from alkaline fusion of the sample solutions. Repeated measurements of the U.S. Geological Survey (USGS) reference materials BHVO-2 ($n = 18$) and AGV-2 ($n = 5$) yielded a reproducibility for all reported major elements in the order of <1%–8% relative standard deviation (RSD).

Trace-Element Analysis

For trace-element concentration analysis, aliquots of digested sample solution were diluted with 5% HNO_3 and doped with In as an internal standard. Trace-element concentrations were determined using an Agilent Technologies 7700 series inductively coupled plasma–mass spectrometer (ICP-MS) operated using the ICP-MS Mass Hunter software package. The calibration curve was obtained using multi-element solutions containing rare earth elements (REEs), large ion lithophile elements (LILEs), and high field strength elements (HFSEs) prepared at the ULB with concentrations varying between below detection limit (blank) and 20 ppb in a 5% HNO_3 solution. Oxide formation was checked and corrected using standard element solutions consisting of Pr and Nd, Ba, and Ce. All standard solutions were doped in an ultrapure lithium metaborate/tetraborate solution to match the matrix resulting from alkaline fusion. Repeated measurements of USGS reference materials BHVO-2 ($n = 17$) and AGV-2 ($n = 5$) yielded reproducibility for the reported trace elements in the order of <1%–10% RSD. Full results for geological reference materials BHVO-2 and AGV-2 are reported in Appendix S1.

RESULTS

Petrography

Crystalline Pre-Impact Material

Modal mineral variations are apparent at the meter scale for both the impactites and the preimpact material, which result in lithological variations. For the pre-impact dikes, we followed the lithological nomenclature used in Morgan et al. (2017), since (re)categorizing the different types of dikes falls outside the scope of this work; variations are described in detail below.

Granitoids. The granitoids are holocrystalline, phaneritic, coarse-grained lithologies, composed of varying quantities of alkali-feldspar, plagioclase, and quartz (each between 20–40 vol%; ±0.5–3 cm) with minor biotite (up to 5 vol%; ±0.2–0.5 cm), and opaque minerals, zircon, titanite, apatite, muscovite, and epidote (<<1 vol%; <0.1 mm) (Fig. S1; see footnote 1). Compositional variations are common between core sections, and in some cases alkali-feldspar dominates, leading to a syenitic composition (Fig. S1A). Textural variations are also common, ranging from roughly equigranular to alkali-feldspar-phyric (with alkali-feldspars up to 7 cm in size). Alteration is pervasive, with epidote and zoisite mineralization. Plagioclase commonly exhibits saussuritization or sericitization, and biotite is extensively chloritized (Figs. S1B–S1C). Shock deformation features are apparent in most rock-forming minerals (i.e., planar fractures and planar deformation features in quartz grains [Fig. S1B], and planar microstructures in plagioclase, titanite, and apatite). No discernible trends or distinct variations in the relative abundance of minerals and texture are observed between in situ granitoids and granitoid clasts.

Dolerites. The dolerites are holocrystalline, equigranular to porphyritic, medium- to fine-grained rocks, with individual dikes having either porphyritic or equigranular textures (Fig. S2; see footnote 1). The porphyritic dolerites vary in mineral content, with the porphyritic minerals ranging from subhedral to euhedral plagioclase (~10–20 vol%; 0.2–1 cm) (Fig. S2A) to clinopyroxene (~10–15 vol%; <0.2–0.4 cm) and/or a granular euhedral mineral (~<<1–5 vol%; <0.2–0.4 mm) that is typically altered to serpentine (Fig. S2B). This mineral is deduced to be altered olivine, based on its euhedral shape and alteration to serpentine. Notably, plagioclase represents the largest and most pervasive phenocrysts (Fig. S2A). The matrix (60–75 vol%) of the porphyritic dolerites varies from a medium-grained inequigranular subophitic texture of subhedral to anhedral clinopyroxene (0.1–0.3 cm) and anhedral (pale-green) amphibole oikocrysts partially or fully enclosing subhedral (more acicular) plagioclase chadacrysts (<1 mm) (roughly 50–10–40 vol%, respectively) to a fine-grained almost cryptocrystalline matrix (grain size around ±20 μm) of equigranular subhedral to anhedral plagioclase and clinopyroxene (roughly 50/50 vol%). Minor phases include ubiquitous opaque minerals (not larger than 100 μm in size) (Fig. S2B). The equigranular dolerites display mineral compositions similar to the porphyritic dolerites but exhibit no clear phenocrysts, with grain sizes not exceeding ~2 mm (Fig. S2C). Alteration is observed throughout, with uralitization of clinopyroxene

to pale-green amphibole and pervasive serpentinization of the inferred olivine (Fig. S2). In some cases (more commonly in the phenocrysts), evidence of shock metamorphism is observed in the form of planar microstructures in plagioclase.

Felsites. The felsites are holocrystalline, medium- to fine-grained lithologies (Figs. S3A–S3B; see footnote 1). Only four felsite dikes have been recovered in Hole M0077A, and these vary texturally from roughly equigranular to locally porphyritic with subhedral to anhedral plagioclase, mostly as acicular laths, although tabular crystals were also observed (<1 mm, generally ±500 μm), potassium feldspar (<1 mm, generally ±500 μm, but aggregates up to 1 cm), and clinopyroxene (<1 mm, generally ±500 μm) that is pervasively altered to chlorite and/or amphibole (Fig. S3B). Modal mineral abundances vary between the different thin sections investigated. Feldspars generally dominate with 50–80 vol%. K-feldspar is typically discernible from plagioclase, as the former is more heavily altered to phyllosilicates, resulting in a mottled appearance (Fig. S3A). However, determining the modal differences between plagioclase and K-feldspars in the total feldspar abundance remains challenging, although plagioclase typically dominates, being close to 80 vol% of the total feldspar content in some cases. Clinopyroxene varies between 10 and 40 vol%, and minor phases generally represent ≤10 vol%; they include anhedral quartz (up to 2 mm) exhibiting shock microstructures, secondary amphibole (rarely up to 1.5 mm), and zoisite (Figs. S3A–S3B). Observed accessory phases include <20 μm subhedral to euhedral epidote and/or apatite (<<1 vol%; see also Gulick et al., 2017b). Quartz grains exhibit a rim of fine-grained crystals at grain boundaries, comparable to a melt-reaction rim, indicating the quartz grains represent entrained mineral clasts from the surrounding granitoid. Zoisite is interstitial, yet it can be enclosed in plagioclase. An unidentified anhedral mineral, which is now altered to fine-grained calcite, is found throughout the felsite lithologies. This mineral can represent up to 50 vol% of the total mineral modal composition (Fig. S3A). One dike contains porphyritic elongated tabular chlorite (up to 3 mm in size) (Fig. S3B), intergrown with opaque mineral phases. Calcite fills veins and vugs throughout the felsites.

Dacites. Dacites form the least prevalent of the pre-impact dikes, with only three identified in the core (Gulick et al., 2017b). They are texturally similar to one another and exhibit a holocrystalline porphyritic texture containing subhedral to euhedral tabular plagioclase (60–70 vol%; up to 5 mm) varying from single crystals to aggregates that are commonly zoned

and exhibit kinked albite twinning (Fig. S3C). Quartz is generally anhedral (20–30 vol%; up to 6 mm) and displays shock microstructures (i.e., several sets of planar deformation features). Biotite is rare (<1–10 vol%; up to 2 mm), displays kink bands, and is typically (partially) altered to chlorite (Fig. S3C). The matrix is composed of inequigranular crystals of subhedral plagioclase, quartz, biotite, and chlorite (±100–600 μm) with modal mineral abundances similar to those of the phenocrysts (Fig. S3C). Accessory phases (<1 vol%) include opaque minerals (±300 μm) and titanite (±200–350 μm).

Impactite Material

Upper impact melt rock: 721.61 until 747.02 mbsf. The upper impact melt rock unit contains two clearly different lithological components: clast-bearing black impact melt rock and green schlieren. The black impact melt rock of the upper impact melt rock unit is an inequigranular, fine- to coarse-grained, hypohyaline to hypocrystalline, clast-bearing impact melt rock, with clast sizes ranging from the centimeter to the meter scale (Figs. 2 and 3A). The matrix varies from isotropic cryptocrystalline to holohyaline, with the former dark brownish–black and the latter ubiquitously altered to brown phyllosilicates (Figs. 3A–3D). The clast types are highly diverse, varying from angular to rounded in shape with crystalline basement fragments of highly weathered, shocked (visible planar deformation features), and generally partially digested granitoid (with up to 70 vol% of total thin section constituting granitoid-derived material) and, more rarely, dolerite clasts (never more than a couple per thin section). The former comprises clasts of <1 mm (Figs. 3A–3C) to up to a few meters in size (Fig. 2), whereas the latter do not exceed ±5 mm. Clasts of mica schist and quartz gneiss documented in the core (Gulick et al., 2017a) have only been observed at the macroscopic scale. Rarely, rounded equant clasts of limestone occur (<0.5 mm; Fig. 3A), which show calcite recrystallization at their margins.

The upper impact melt rock unit also includes isolated anhedral to subhedral quartz, plagioclase, K-feldspar, and clinopyroxene mineral clasts, which vary in size from ≤100 μm to a few millimeters (Figs. 2, 3A, and 3C). Crystalline clasts can exhibit embayment features and commonly display reaction rims, recognizable as rounded edges of the crystals (Fig. 3B), implying reaction with the matrix material. Locally, the matrix contains small (<50 μm) euhedral acicular plagioclase (70–80 vol%) and subhedral to anhedral equant pyroxene microlites (20–30 vol%) (Figs. 3A–3C). The plagioclase crystals display a trachytic to intersertal (or hyalopilitic) texture (Fig. 3C), with plagioclase

in subparallel alignment, though radial (spherulitic) textures are also observed (Fig. 3B, in the embayment feature). Both plagioclase and pyroxene microlites are present in embayment features in granitoid clasts. These textural observations indicate that microlites crystallized from the impact melt, whereas larger crystalline material (>0.5 mm; Figs. 3B–3D) was likely derived from the target rock. Rarely perlitic cracks can be observed in the matrix. Vesicles, amygdules, and veins, typically filled with calcite, are ubiquitous throughout the upper impact melt rock material (Fig. 3C).

The green schlieren, which are pervasive throughout the top of the upper impact melt rock unit between 721.61 and 737.56 mbsf, display macroscopic textures that vary from being more brecciated, where black impact melt rock clasts incorporated into the green schlieren are angular, to features where both lithologies appear to mingle, hinting at immiscibility between the two lithologies (Figs. 2 and 3D). On the microscale, these schlieren are fine-grained cryptocrystalline material that is distinctly lighter gray in plane-polarized light relative to the black impact melt rock (Fig. 3D). The green schlieren contain clasts of dark-brown, fully isotropic, angular to subrounded fragments (<100 μm) that exhibit a blebby texture, likely representing fine-grained glassy fragments of impact melt rock now altered to phyllosilicates. Strikingly, the green schlieren exhibit pervasive calcite crystallization with subhedral to anhedral crystals, from microcrystalline to >1 mm, throughout the impact melt rock unit (Fig. 3D). The fine-grained cryptocrystalline material lines the contact with black impact melt rock, whereas the centers of the schlieren are commonly recrystallized to comparatively massive calcite. The massive calcite is interpreted to be secondary, as commonly observed throughout all lithologies of the Hole M0077A core (Gulick et al., 2017a, 2017b). Importantly, the green schlieren in the upper impact melt rock unit are clearly dissimilar to the vesicles, veins, and amygdules that are pervasive throughout the upper section of the upper impact melt rock unit.

Lower impact melt rock–bearing unit: Between 917.17 and 1334.69 mbsf. The lower impact melt rock–bearing unit is broadly characterized by an inequigranular hypocrystalline to holocrystalline brecciated texture, with a near-continuous grain-size distribution from fine-grained (cryptocrystalline) to coarse-grained (hypocrystalline) brecciated granitoid basement rock, containing both impact melt rock clasts and a multitude of crystalline basement–derived material (Figs. 2 and 3E–3G). In the coarser-grained material, patches that are clearly isotropic indicate the presence of fine-grained vitric particles in the matrix (Figs. 3E–3G). However,

the majority of the matrix appears to be composed of fragmented basement material and impact melt rock fragments (Fig. 3). On the macroscale, the latter can be identified as black patches, whereas the former is blackish-gray (Fig. 2, lower impact melt rock–bearing unit).

The lower impact melt rock–bearing unit contains a variety of clasts and clast sizes, varying from small singular, basement-derived crystals (<1 mm) to angular and subangular basement clasts, up to a few centimeters in size (Fig. 3E), and up to a few meters at the macroscopic scale (Fig. 2). At the microscopic scale, these basement clasts can show melt coating (Fig. 3E). Clasts include granitoid material exhibiting saussuritization of the plagioclase, and shock metamorphic features (planar deformation features and [less commonly] diaplectic glass), equigranular-textured dolerite, mica schist, and quartz gneiss (similar to the lithologies described in Gulick et al., 2017b). Individual crystals in the matrix do not show embayment features or reaction rims, implying fragmentation of this material by a mechanical process, which is in agreement with earlier observations on the lower impact melt rock–bearing unit (Riller et al., 2018).

Throughout the lower impact melt rock–bearing unit, altered vitric clasts are observed, which are similar to the melt rock in the upper impact melt rock unit; they are fragmental and contain angular basement clasts in a brown holohyaline (Fig. 3F) to dark brownish–black cryptocrystalline (Fig. 3G) matrix. The holohyaline clasts appear more globule-like, showing a fluidal texture (Fig. 3F), whereas the cryptocrystalline clasts are generally angular (Fig. 3G). Both types of melt clasts mostly contain individual basement-derived crystals (feldspars, quartz, and rare clinopyroxene; Figs. 3F and 3G). When compared to the upper impact melt rock unit, the lower impact melt rock–bearing unit does not contain sedimentary clasts, hardly displays any vesiculation or amygdules, and exhibits limited to no calcite crystallization. Euhedral iron sulfides (possibly pyrite) are concentrated in the matrix and at grain boundaries but are not found enclosed in clasts or other crystal phases.

Geochemistry

Whole-Rock Elemental Compositions

Owing to the large variation in loss on ignition (LOI) between the different studied lithologies, varying from <1 wt% in the case of the crystalline target rocks up to >30 wt% for the limestone clasts (see Appendix S1), all data presented here were recalculated on a volatile-free basis, with total iron expressed as ferrous oxide (FeO*). As the target rock is mostly composed
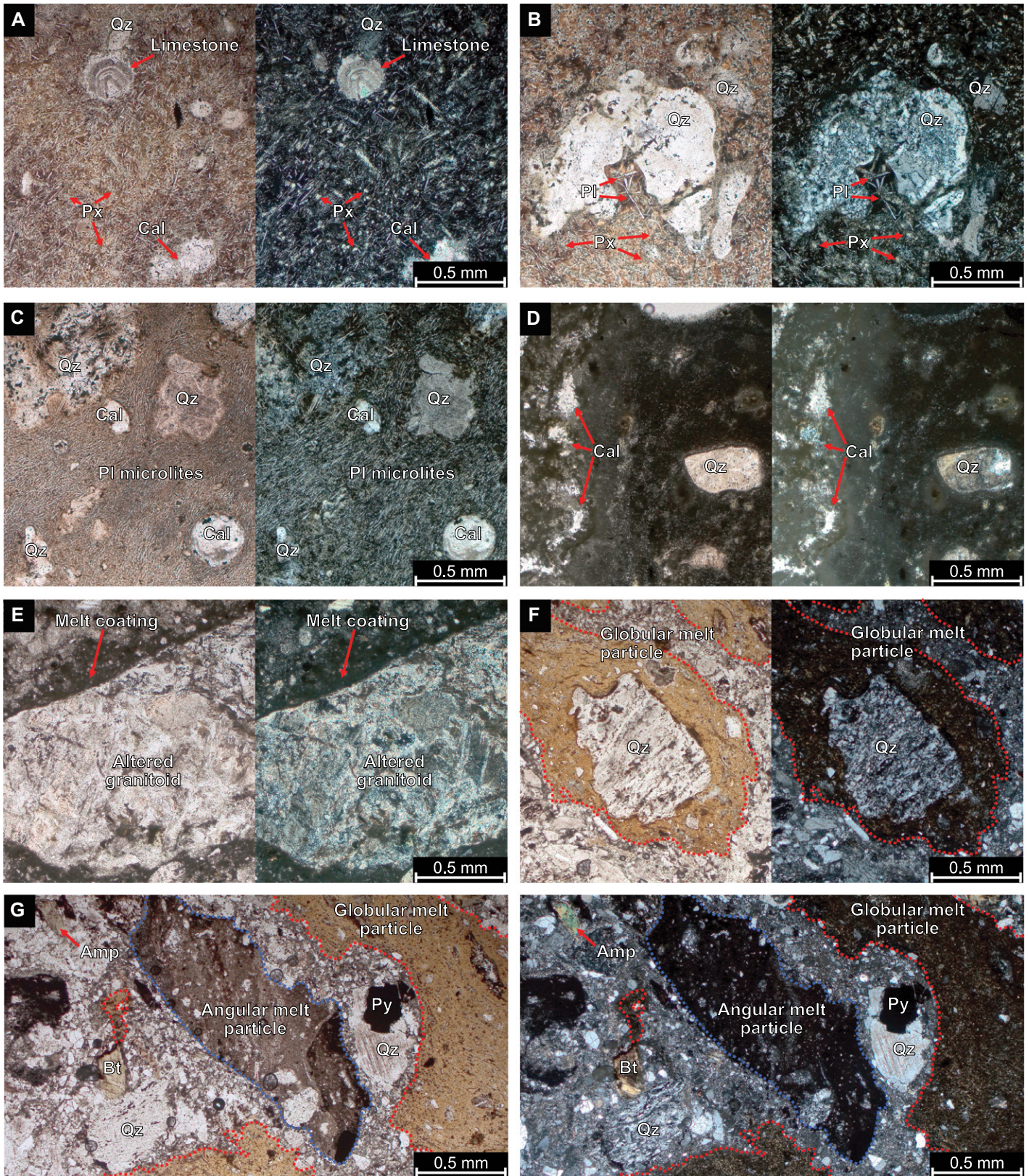
Figure 3. Representative thin sections of impact melt rock units in plane-polarized light (left) and cross-polarized light (right). (A) Upper impact melt rock (95_1_52_54) with limestone clasts and characteristic plagioclase and pyroxene microlites, where the former are observed as white acicular laths throughout the thin section. (B) Upper impact melt rock (95_1_52_54) with a granitoid basement clast with embayment features, in which we can observe intersertal radial plagioclase. (C) Upper impact melt rock (100_1_57_79) with plagioclase microlites in trachytic alignment, indicating flow around entrained basement clasts. At the bottom right, an amygdule is visible. (D) The interaction between green schlieren (left) and black melt (right) in the upper impact melt rock (89_1_57_59). (E) Basement clast in the lower impact melt rock–bearing unit (192_1_56_58) with melt rim (coat) around the clast. (F) Globule-like melt particles with an entrained basement clast (highlighted in red) in the lower impact melt rock–bearing unit (282_1_80_82). (G) Lower impact melt rock–bearing unit (282_1_80_82) showing angular (blue) and globule-like melt particle (red) next to one another and with fragmented basement material around it. Quartz with shock deformation features is visible in between the melt particles. Amp—amphibole; Bt—biotite; Cal—calcite; Pl—plagioclase; Px—pyroxene; Py—pyrite; Qz—quartz. Mineral abbreviations from Whitney and Evans (2010).

◄────────────────────

of silicate rock, this method allows for a better disentanglement of the possible contributions from the silicate rock precursors to the impactite mixtures. Non-recalculated major-element data of all pre-impact lithologies are provided in Appendix S1.

Pre-impact lithologies. The granitoids ($n = 24$) examined in this study document the most felsic lithology sampled in the Hole M0077A core, with distinct variations in major-element content, varying from evolved to highly evolved alkaline granites with high total alkalis ($Na_2O + K_2O$) and SiO_2 contents of 7.4–10.5 wt% and 70.6–78 wt%, respectively. A single exception records a syenitic composition with the highest total alkali (13.42 wt%) and lowest SiO_2 (68.57 wt%) contents recorded in the granitoid sample suite (Fig. 4). The granitoids have comparatively low CaO (0.7–3.2 wt%), FeO* (0.4–2.4 wt%), TiO_2 (0.1–0.6 wt%), and MgO (0.1–1.2 wt%) contents that highlight an evolved nature (Fig. 4). With the exception of the syenitic composition (17.3 wt% Al_2O_3), Al_2O_3 shows a decreasing trend, varying from 15.3 to 11.8 wt%, with increasing SiO_2 (Fig. 4). No significant differences are observed between in situ granitoids and granitoid clasts in terms of their major-element contents, with both sample groups clustering together. In terms of trace-element concentrations, the granitoids are very similar to each other, exhibiting enriched compositions, with most reported trace elements above 10 times CI-chondrite values and extending to >1000 times in the case of fluid-mobile elements such as Ba, Th, and U (Fig. 5A) for specific granitoid clasts. Moreover, both groups of granitoids generally show relative Nb and Ta depletion and moderate Zr and Hf enrichment relative to neighboring trace elements, typical of arc-type magmatism (Pearce et al., 1984). Light rare earth element (LREE) concentrations higher than 10 times CI-chondrite, heavy rare element (HREE) concentrations below 10 times CI-chondrite, minor negative Eu anomalies, and Lu enrichment relative to Yb characterize most of the granitoids (Fig. 5A). Interestingly, two granitoid clasts show HREE compositions distinctly more enriched than the other granitoids (Fig. 5; >10 times CI-chondrite), with one showing strong LREE enrichment, and the other exhibiting distinct Zr and Hf enrichments (Fig. 5A). These variations might reflect either compositions affected by impact melt interaction or entirely distinct types of granitoid.

The dolerites ($n = 13$) reflect the most mafic lithology sampled in this study, documenting generally gabbroic compositions with low total alkalis and SiO_2 contents (between 2.5–4.1 wt% and 44.6–49.2 wt%, respectively). The exception is one sample extending to slightly higher total alkalis and SiO_2 contents (5.7 and 50.8 wt%, respectively), displaying a monzogabbroic composition (Fig. 4). Conversely, the dolerites record higher but more variable contents of CaO (2.6–11.2 wt%), FeO* (10.7–16.1 wt%), TiO_2 (0.9–2.1 wt%), and MgO (9.5–17.7 wt%), relative to the felsic granitoids (Fig. 4). An opposite trend for Al_2O_3 is shown when compared to the granitoids, with an increase in Al_2O_3 with increasing SiO_2, varying from 14.5 to 17.5 wt% (Fig. 4). In terms of CI-chondrite–normalized trace-element composition, the dolerites display little variation, with a generally flat trace-element signature, and with most reported elements plotting between 10 and 100 times CI-chondrite concentrations (Fig. 5B). Variations are observed in the enrichment of fluid-mobile elements Ba and U and depletion of Pb for most samples. Yb exhibits a slight negative anomaly relative to Er and Y for all samples.

The felsites ($n = 4$) have more intermediate monzonitic compositions with high total alkalis and intermediate SiO_2 contents (7.7–8.3 and 57.4–59.7 wt%, respectively; Fig. 4). Most major-element contents plot in between the gran-

itoid and doleritic lithologies, in terms of CaO (4.4–6.6 wt%), FeO* (4.4–6.6 wt%), TiO_2 (0.6–0.9 wt%), and MgO (3.6–5.9 wt%). The Al_2O_3 content varies between 15.2 and 16.2 wt% and does not vary conversely with SiO_2, although this relationship cannot be noted with certainty as the sample suite is limited (Fig. 4). Importantly, the felsites reflect the most trace-element–enriched lithology documented so far in the Hole M0077A core, with most elements displaying ≥100 times CI-chondrite concentrations and Ba, Th, U, La, and Ce contents being upwards of 1000 times CI-chondrite values (Fig. 5C). All felsites are characterized by depletions in Nb, Ta, Pb, Sr, Zr, and Hf contents relative to neighboring trace elements (Fig. 5C).

The dacites ($n = 3$) sample a more evolved lithology strongly comparable to the granitoids, except for slightly lower SiO_2 content (between 67.8 and 70.7 wt%) (Fig. 4). These samples document quartz monzonitic to granitic compositions, plotting close to the granodiorite-quartz monzonite-granite triple junction (Fig. 4), with total alkalis between 8.4 and 9.6 wt%. CaO (1.8–2.1 wt%), FeO* (2.2–2.7 wt%), TiO_2 (~0.4 wt%), and MgO (1–1.2 wt%) contents are similar to those of the granitoids, falling in the same range for most elements (Fig. 4). For Al_2O_3 data, no covariation with SiO_2 contents (varying between 14.6 and 15 wt%) is observed, although the sample set is limited. The trace-element compositions are very similar to those of the granitoids, exhibiting enriched compositions, with most reported trace elements above 10 times and up to >800 times CI-chondrite values for fluid-mobile element U in a single sample (Fig. 5D). Furthermore, the dacites display relative Nb, Ta, and Pb depletion and moderate Zr and Hf enrichment when compared to neighboring trace elements (Fig. 5D). The minor negative Eu anomalies that characterize most of the granitoids are absent in the dacites, marking them as a different lithology.

The limestones ($n = 2$) represent the only sedimentary rocks sampled in this study. Both samples were taken from the transitional interval between the suevite and the upper impact melt rock unit (near the Unit 2-3 boundary). The limestones document major-element compositions with high CaO (~90% wt%) and low MgO (~3 wt%) and SiO_2 (~5 wt%) contents, while all other major elements account for <2 wt% (Appendix S1). Most trace-element concentrations fall below 2 ppm, with the exception of Ba (up to 1000 ppm), Sr (up to 600 ppm), high La (up to 43 ppm), Ce (up to 37 ppm), Y (up to 17 ppm), and Nd (up to 12 ppm) (Appendix S1). As the majority of the major- and trace-element abundances of these limestone samples are very low, they were not
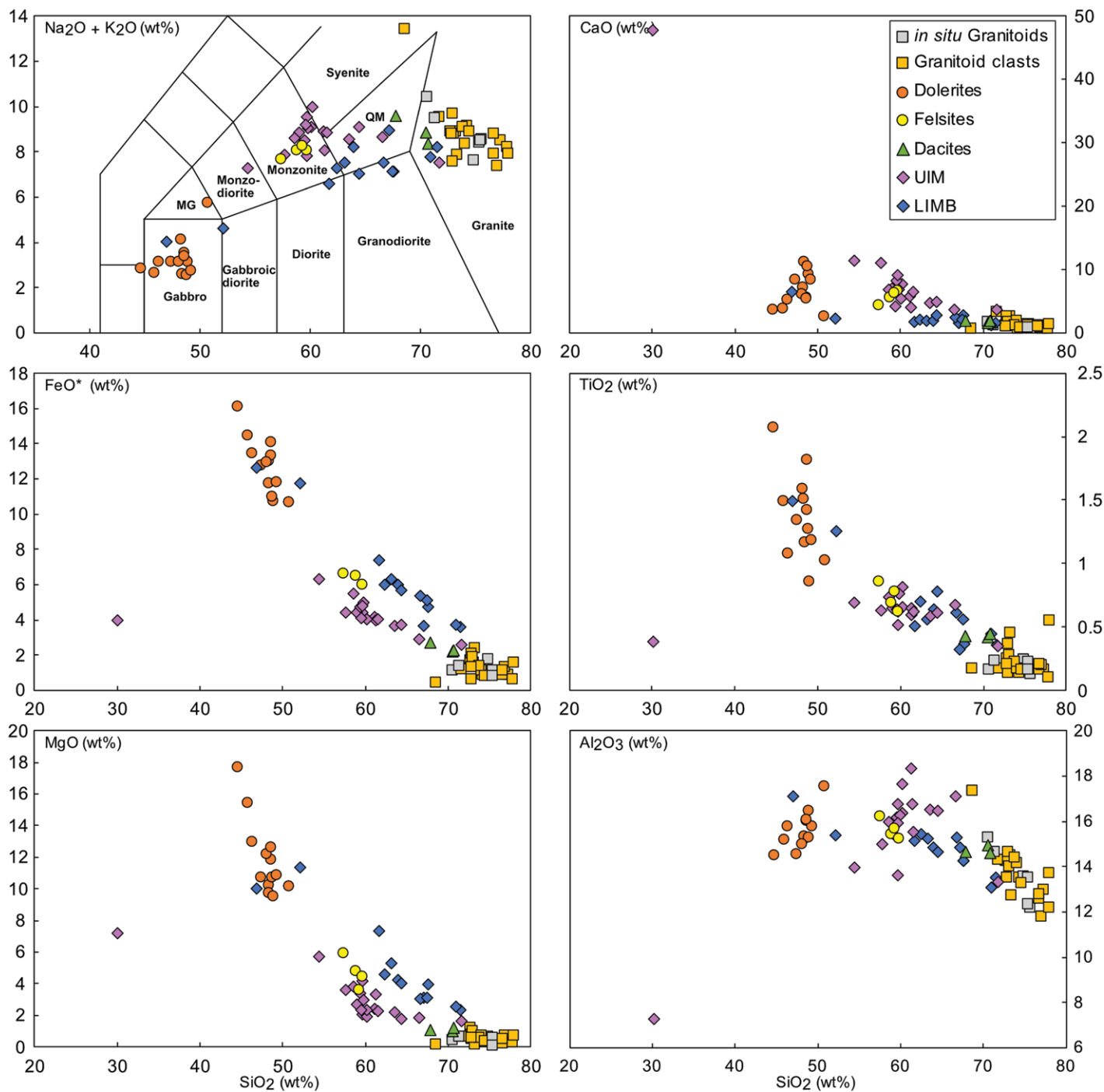
Figure 4. Major-element compositions plotted against SiO₂ (wt%), with all Fe expressed as total ferrous oxide (FeO*). All data were recalculated on a volatile-free basis. Total alkali–silica (TAS) diagram (top left) is after Le Maitre et al. (2005) with syenite and quartz monzonite fields from Middlemost (1994); MG—monzogabbro; QM—quartz monzonite. UIM—upper impact melt rock unit; LIMB—lower impact melt rock–bearing unit.

included in the Harker diagrams or normalized trace-element diagrams (Figs. 4 and 5).

Impactite lithologies. For the impactites, significant outlier samples exist, which are related to potential sample bias and heterogeneity at the centimeter scale (see petrography

in Gulick et al., 2017a, 2017b). The data presentation is therefore expanded to also provide the mean and two sigma standard deviation (2σ) (Appendix S1).

The upper impact melt rocks (*n* = 19) record clear variation in total alkalis, SiO₂, and CaO con-

tents, varying 7.3–10 wt% (8.6 ± 1.4 wt%), 54.4–71.7 wt% (61 ± 7.5 wt%), and 3.6–11.4 wt% (6.6 ± 4.6 wt%), respectively (Fig. 4), although sample 87_2_73_75 represents an outlier with 3 wt% total alkalis, 30.1 wt% SiO₂, and 47.8 wt% CaO. This sample is part of the earlier
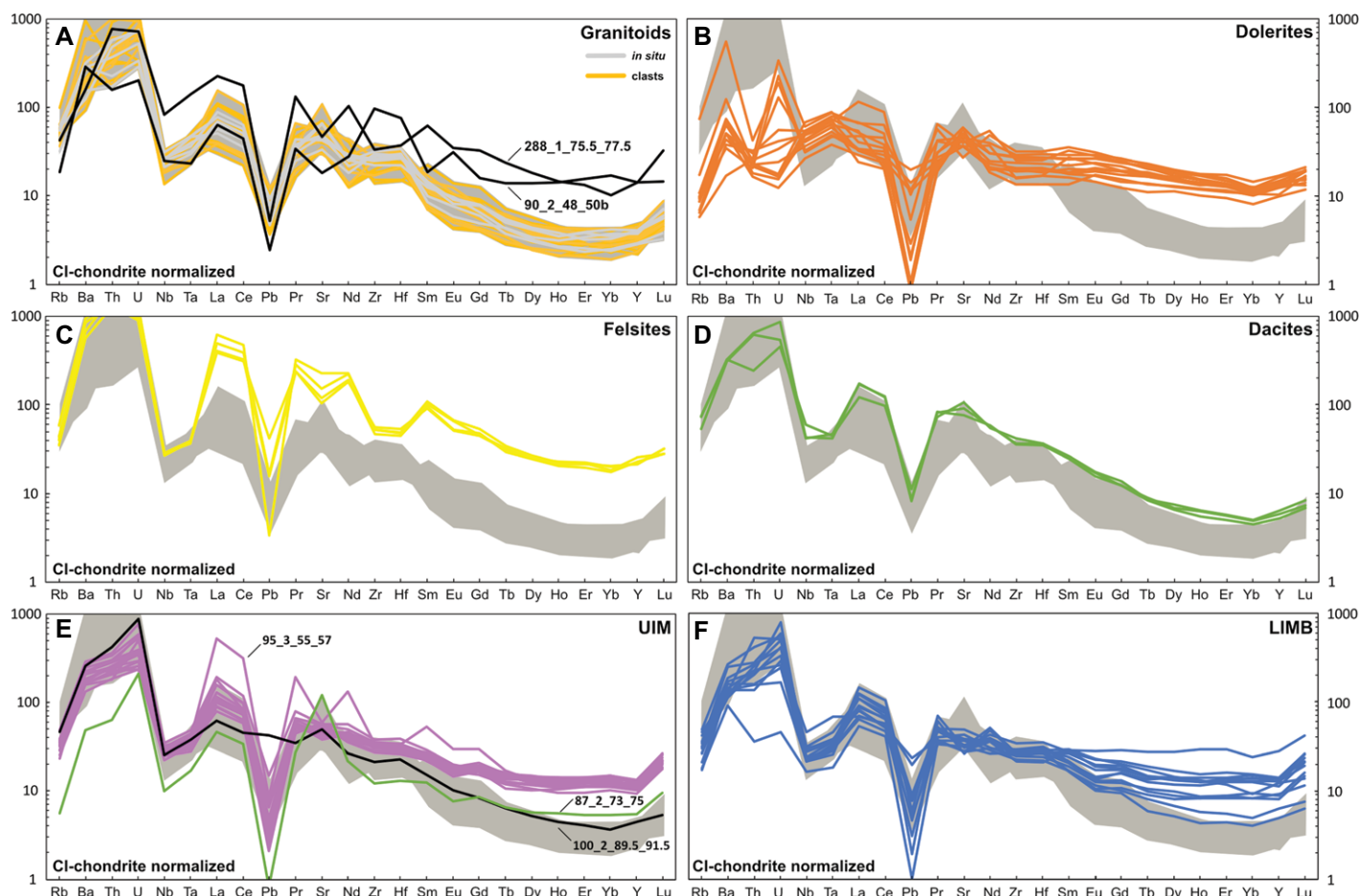
Figure 5. CI-chondrite–normalized trace-element concentrations, with normalization values from Sun and McDonough (1989). Gray outline in all panels reflects the majority of granitoids, excluding the outlier samples shown in A. (A) Granitoids, where black lines reflect outlier samples. (B) Dolerites. (C) Felsites. (D) Dacites. (E) Upper impact melt rock unit (UIM), highlighted in green is a green schlieren sample, highlighted in black is a sample representing the contact between impact melt rock and granitoid. (F) Lower impact melt rock–bearing unit (LIMB).

described green schlieren lithology (Fig. 2) and is therefore not included in the mean. The FeO* (2.6–6.3 wt%; 4.3 ± 1.7 wt%), TiO$_2$ (0.4–0.8 wt%; 0.6 ± 0.2 wt%), Al$_2$O$_3$ (13.3–18.3 wt%; 16 ± 2.7 wt%), and MgO (1.6–5.7 wt%; 2.8 ± 2.1 wt%) values are significantly lower, recording intermediate compositions when compared to magmatic target lithologies (Fig. 4). The lower impact melt rock–bearing samples ($n = 13$) display generally less variation for most major elements, with total alkalis and SiO$_2$ contents varying (4–8.9 wt%; 7.1 ± 2.7 wt%) and (46.9–71.5 wt%; 63.5 ± 14 wt%), respectively (Fig. 4). The CaO (1.3–6.5 wt%; 2.4 ± 2.7 wt%), FeO* (3.6–12.6 wt%; 6.3 ± 5.7 wt%), TiO$_2$ (0.3–1.5 wt%; 0.7 ± 0.7 wt%), Al$_2$O$_3$ (13.1–17.1 wt%; 14.9 ± 2 wt%), and MgO (2.3–11.4 wt%; 5 ± 5.7 wt%) contents are generally slightly more mafic than the upper impact melt rock unit and are most comparable to the dolerites in major-element content (Fig. 4).

Trace-element compositions display limited variation between the impactites, with a comparable CI-chondrite–normalized pattern for most elements (Figs. 5E–5F). These patterns are characterized by more enriched compositions, with most reported trace elements between 10 and 100 times CI-chondrite values (Figs. 5E–5F). Fluid-mobile elements Ba, Th, and U, and the elements La, Ce, and Sr are the only observed elements to exceed 100 times CI-chondrite values (Figs. 5E–5F). The middle rare earth elements (MREEs) to HREEs fall below 10 times CI-chondrite values in a few upper impact melt rock unit and lower impact melt rock–bearing unit samples (Figs. 5E–5F). Exceptions to these observations are documented in three upper impact melt rock unit samples and the lower impact melt rock–bearing unit as a whole, showing more variation in HREE content (Fig. 5F) and varying between 6 and 40 times CI-chondrite values. These three

upper impact melt rock unit samples include the green schlieren sample 87_2_73_75, which displays the highest Sr concentration (885 ppm) of all upper impact melt rock unit samples but the lowest concentrations for most other elements (Fig. 5E). Sample 95_3_55_57, which exhibits a CI-chondrite–normalized pattern with distinct La, Ce, Pr, Nd, Sm, and Gd enrichment, most comparable to the elemental signature of the felsites. Lastly, sample 100_2_89.5_91.5, highlighting an interaction zone between granitoid and the upper impact melt rock unit (Fig. 2), displays the second lowest compositions for most trace elements, but with distinctly high Pb concentrations compared to all other sample groups (Fig. 5E).

Incompatible Element Composition

Pervasive alteration of both pre- and post-impact lithologies is apparent throughout the Chicxulub impact structure (Ames et al., 2004;

Zürcher and Kring, 2004; Wittmann et al., 2004; Gulick et al., 2017a, 2017b; Kring et al., 2020) and could have affected whole-rock compositions, especially in the case of mobile elements. Moreover, the Hole M0077A core contains an abundance of different lithologies formed in different geological settings. Incompatible element compositions and ratios are less affected by alteration and make it possible to distinguish between different melting regimes (anhydrous or hydrous) (e.g., Pearce et al., 1984; Pearce, 2014). The HFSEs Zr, Ta, Th, and Hf are incompatible in silicate phases, thus a linear relation between the concentrations of these elements is expected. When plotted against Hf concentrations, a strong correlation with Zr is observed for all sample groups (Fig. 6A), with Zr and Hf varying from 50 to 214 ppm and from 1 to 6 ppm, respectively. Of the impactites, the upper impact melt rock unit records the highest Zr and Hf concentrations in the core, up to 146 ppm and 4.12 ppm, respectively. The dolerites, dacites, and granitoids tend to overlap, with the exception of granitoid clast sample 90_2_48_50b, which records the highest values of Zr (373 ppm) and Hf (7.99 ppm) (Fig. 6A). The felsites yield more enriched val-

ues, plotting around 200 ppm Zr and 5 ppm Hf (Fig. 6A). The Ta and Th concentrations show more scatter, with only the dolerites exhibiting covariation between Ta and Hf (Fig. 6B) and only the felsites exhibiting covariation between Th and Hf (Fig. 6C). The Ta values are generally comparable for all lithologies with concentrations below 1 ppm, but no covariation is observed for both granitoid groups and impactites (Fig. 6B). Th contents are most noticeably scattered for the granitoids, whereas the values for the lower impact melt rock–bearing unit and upper impact melt rock unit cluster closer together (Fig. 6C).

Ratios of Th/Yb versus Nb/Yb and Rb versus Y + Nb can be used to fingerprint the tectonic settings of ophiolites (Pearce, 2014) and granitic rocks (Pearce et al., 1984), respectively. While not commonly used in impact cratering studies, these ratios are able to highlight the clear differences between target lithologies and allow insight into their formation, while simultaneously pointing out the similarities between the impactite units. Highly incompatible elements Th and Nb exhibit similar behavior in an anhydrous mantle melting system, resulting in a linear relationship between

the Th/Yb and Nb/Yb ratios (Fig. 7A; Pearce, 2008, 2014). However, in a hydrous subduction environment, Th and Nb become decoupled as slab-derived fluid metasomatism is able to mobilize Th but not Nb. Only the dolerites record anhydrous mantle–derived compositions, clustering around enriched mid-ocean-ridge basalt (E-MORB; Fig. 7A). All other sample groups are significantly enriched in Th relative to Nb, with the impactites, felsites, and granitoids + dacites showing isolated clusters. Exceptions exist, with one granitoid sample plotting close to the impactites, and one upper impact melt rock unit and five lower impact melt rock–bearing unit samples recording deviations from the majority of the impactite compositions (Fig. 7A). For the Rb versus Y + Nb concentrations, mantle heterogeneities affect Rb and Nb equally, while Y remains unaffected (Pearce et al., 1984). These elements show more scatter for the sample groups, generally caused by variations on the abscissa, with one dolerite and two granitoid clast samples plotting away from their respective sample groups (Fig. 7B). With the exception of granitoid sample 285_3_33_35, all lithologies plot in the volcanic arc field, although the lateral
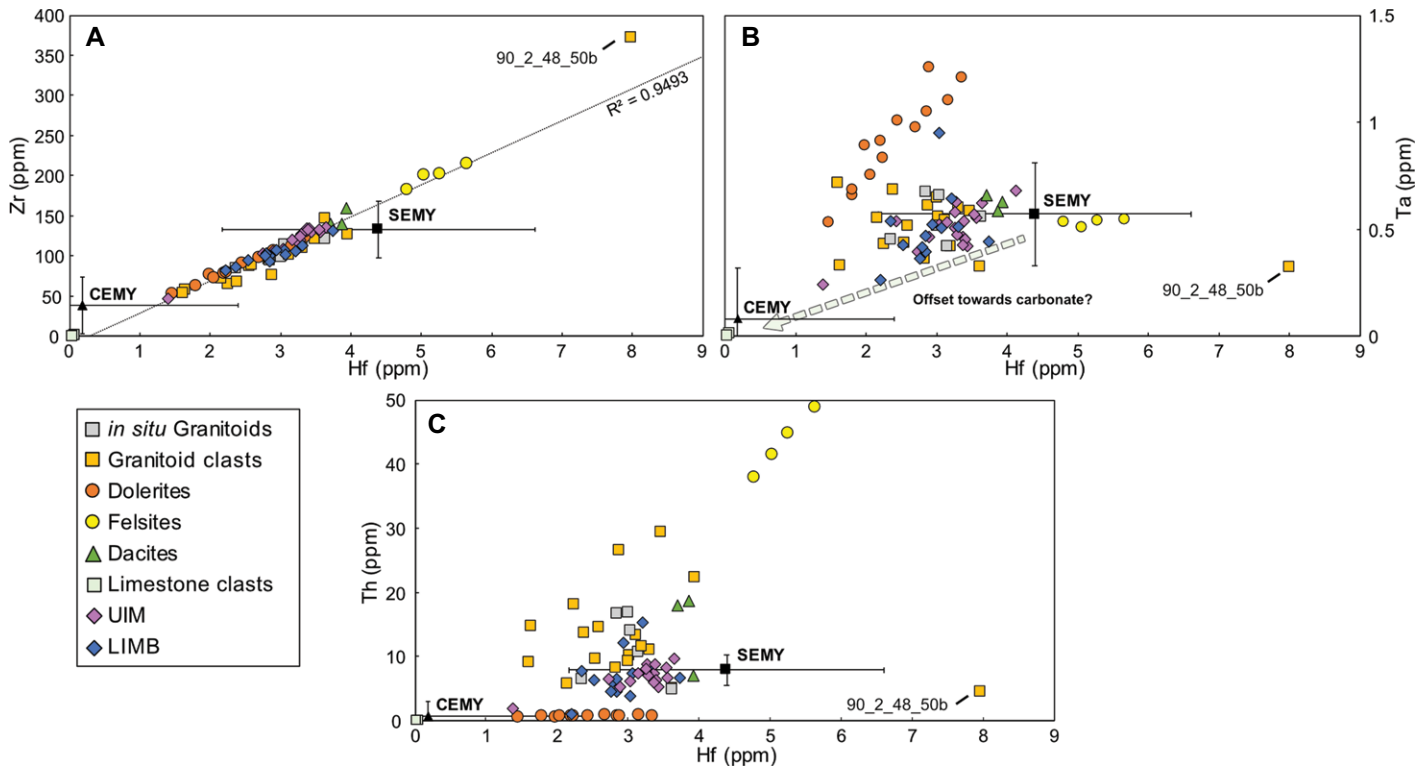

Figure 6. Plots for selected high field strength elements. (A) Zr vs. Hf, where dotted line represents the trend line calculated for all data points with the exception of the limestones and outlier sample 90_2_48_50b. (B) Ta vs. Hf. (C) Th vs. Hf. SEMY—siliceous end member of the Yax-1 impactites from Tuchscherer et al. (2005); CEMY—carbonate end member of the Yax-1 impactites from Tuchscherer et al. (2005). These compositions reflect the impact melt rock and Ca-carbonate target rock end-member compositions calculated from the Yax-1 impactites. UIM—upper impact melt rock unit; LIMB—lower impact melt rock–bearing unit.
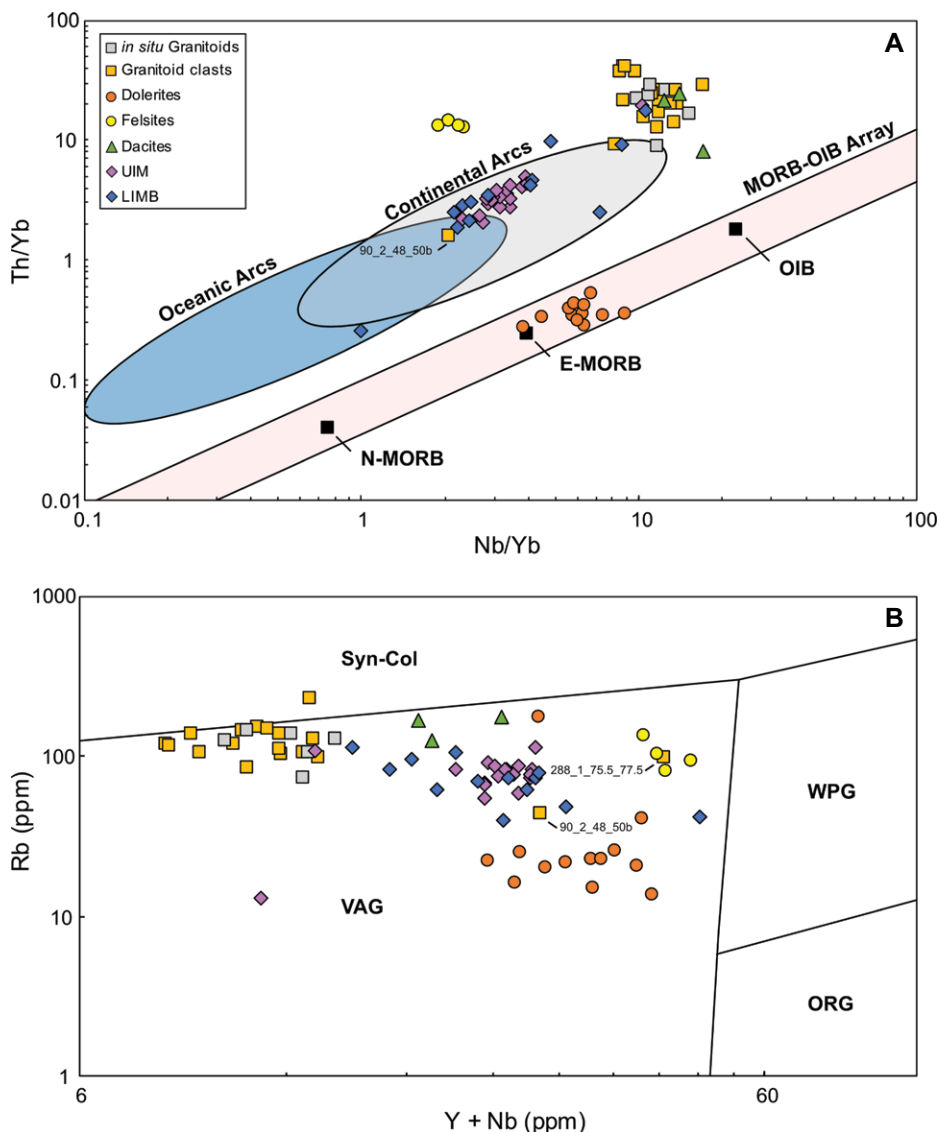
Figure 7. (A) Th/Yb vs. Nb/Yb. Fields after Pearce (2014). (B) Rb vs. Y + Nb. Fields after Pearce et al. (1984). MORB—mid-ocean-ridge basalt; N-MORB—normal mid-ocean-ridge basalt; E-MORB—enriched mid-ocean-ridge basalt; OIB—ocean-island basalt; Syn-Col—syncollisional granite; WPG—within-plate granite; VAG—volcanic arc granite; ORG—orogenic granite; UIM—upper impact melt rock unit; LIMB—lower impact melt rock–bearing unit.

scherer et al., 2006; Kring et al., 2020; this study), likely under the influence of a long-lived (up to 10 m.y.) hydrothermal system (Abramov and Kring, 2007; Osinski et al., 2020; Kring et al., 2020). It stands to reason that this alteration accommodated remobilization of fluid-mobile elements, such as K (Hecht et al., 2004). Trace-element variations are primarily controlled by primary differentiation processes and/or remobilization as a result of hydrothermal fluids. The covariation of fluid-immobile trace elements Zr and Hf (Fig. 6A) indicates that variations in these elements were modified by primary differentiation processes and not remobilization, allowing covariations with these elements to be used as an indication of the extent of alteration of other trace-element contents (Fig. 8A).

The granitoids show no significant covariation in La and Zr concentrations, essentially indicative of the complete decoupling of the two elements, with the R^2 value being close to zero (Fig. 8A). In the other lithologies (even the impactites), covariation in La and Zr is more apparent, with an R^2 value up to 0.27 for the dolerites (Fig. 8A). This decoupling of La from immobile element variations is exacerbated when comparing the CI-chondrite–normalized ratios of LREEs over the HREEs, shown here as $(La/Yb)_N$, to variations in Yb_N concentrations (Fig. 8B). Significant variations in $(La/Yb)_N$ at similar Yb_N contents for the granitoids and dacites, with some granitoid clasts extending to $(La/Yb)_N > 30$, indicate remobilization of La, whereas the similar $(La/Yb)_N$ ratios at varying Yb_N contents for the upper impact melt rock unit, lower impact melt rock–bearing unit, and dolerites indicate less remobilization (Fig. 8B). When using SiO_2 as a proxy for differentiation on the abscissa (Fig. 8C), similar patterns emerge, and there appears to be no covariation between $(La/Yb)_N$ and SiO_2 (wt%) for the granitoids, implying that these variations were not a result of differentiation (Fig. 8C). Another important observation is that the limestone clasts display abnormally high La contents, comparable to those of the granitoids (Fig. 8B). This observation strongly argues that La, and thus, similarly, other more fluid-mobile elements, have been remobilized in the Chicxulub impact structure.

It is important to note that the granitoids appear to have been most affected by alteration. The pervasive shock metamorphism and fracturing observed in the bulk of the granitoid samples from the Hole M0077A core (e.g., Morgan et al., 2016; Riller et al., 2018; Rae et al., 2019; Feignon et al., 2020; this study) explains the propensity of these rocks to be more pervasively altered than the other lithologies. Interestingly, the granitoid clasts vary, displaying both the lowest and the highest La/Yb ratios observed

variations of the sample groups relative to the granitoids imply a mantle signature for the dolerites (lower Rb, but higher Y + Nb than the granitoids) and an enriched crustal signature for the felsites (similar Rb, but higher Y + Nb than the granitoids) (Fig. 7B). Variations on the abscissa are mostly caused by higher Nb values for the dolerites (up to 15 ppm), whereas felsites display much higher Y concentrations (up to 40 ppm). For all reported trace-element compositions and ratios, most of the impactites are constrained between the compositions of the pre-impact lithologies (Figs. 5–7).

DISCUSSION

Hydrothermal Alteration within the Chicxulub Structure

The pervasive alteration of the Chicxulub impact structure lithologies is apparent in the form of widespread alteration of vitric melt particles to phyllosilicates, chloritization and serpentinization of mafic minerals, subsequent conversion of chlorite to phyllosilicates, and extensive calcite crystallization in veins (Hecht et al., 2004; Zürcher and Kring, 2004; Tuch-
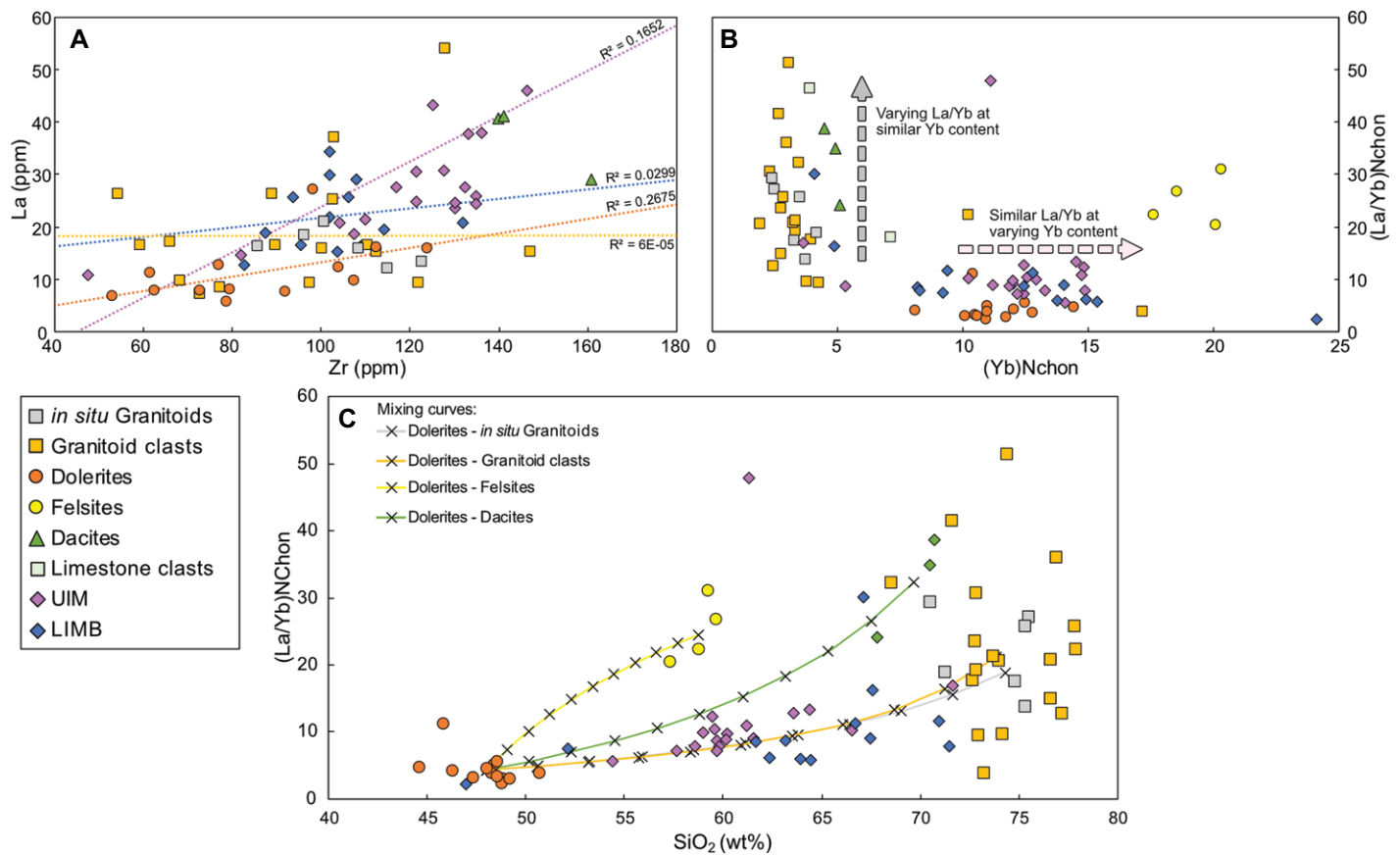
Figure 8. (A) La vs. Zr, where dotted lines represent the trend line calculated for each data set, excluding dacites and felsites due to small sample group size. (B) $(La/Yb)_{Nchondrite}$ vs. $Yb_{Nchondrite}$. (C) $(La/Yb)_{Nchondrite}$ vs. SiO_2 with normalizing values from Sun and McDonough (1989). Mixing lines were calculated between averaged compositions of the different lithologies and averaged dolerite compositions. Each cross represents 10% mixing. UIM—upper impact melt rock unit; LIMB—lower impact melt rock–bearing unit.

in the Hole M0077A core. This observation suggests, but does not conclusively assert, that isolated clasts in the impactite units were more affected by alteration when compared to the bulk of the intersected granitoid in Hole M0077A. Nonetheless, all sampled lithologies have been affected by alteration, and care has to be taken when considering variations in elements typically associated with metasomatism. Our further interpretation of the geochemical data is therefore focused on variations of the more immobile trace elements.

Characteristics of the Pre-Impact Lithologies

Detailed descriptions of the pre-impact lithologies are mostly based on ejecta material and clasts sampled from impactites recovered by drill core projects (e.g., Koeberl, 1993; Tuchscherer et al., 2005) rather than in situ samples (e.g., Zhao et al., 2020). As such, it becomes imperative to geochemically characterize the pre-impact lithologies sampled in the Hole

M0077A core before being able to compare these lithologies to the geochemical composition of the upper impact melt rock unit and lower impact melt rock–bearing unit.

In total, five pre-impact lithologies that could have contributed to the impact melt were sampled: granitoid, dolerite, felsite, dacite, and limestone. The granitoids are characterized by decreasing Al_2O_3 with increased differentiation, commonly associated with fractionation of plagioclase (Langmuir et al., 1992; Sisson and Grove, 1993). However, the overall high Al_2O_3 content indicates the partial retention of plagioclase, which is a common characteristic of hydration of the source region (Sisson and Grove, 1993). Interestingly, the small negative Eu anomaly observed in some granitoids (Fig. 5A) argues against significant plagioclase accumulation (Taylor and McLennan, 1981), indicating that these granitoids reflect intrusions rather than cumulates. On the other hand, the HREE Lu enrichment relative to the MREE Yb points to the melting of garnet in the source region (e.g., Novak and Gibbs, 1971; van

Westrenen et al., 2001) and, together with the Nb and Ta depletions, strongly indicates an arc-like signature (e.g., Sisson and Grove, 1993) for the bulk of the granitoid. This arc affinity is further substantiated by the Th/Yb, Nb/Yb, Rb, and Y + Nb variations (Fig. 7; Pearce et al., 1984; Pearce, 2014). The notably high Th and Nb contents further indicate a continental volcanic arc as the tectonic setting in which the bulk of the granitoids formed (Fig. 7). Previous research has suggested the granitoids reflect an adakitic lithology based on their anomalously high La/Yb ratio (Zhao et al., 2020; see also Fig. 8). However, the enrichment in La is likely related to alteration rather than being a primary signature (Fig. 8), as demonstrated in the previous section. As such, it is interpreted that the geochemical composition of these granitoids indicates they are non-adakitic continental arc–derived intrusions, which fits with the Carboniferous age and tectonic history presented in Ross et al. (2021). Lastly, the geochemical variation observed in granitoid clast samples 90_2_48_50b and 288_1_75.5_77.5 (Figs. 5–7) when compared

to the bulk of the granitoid samples cannot be simply explained through alteration (Fig. 8). As such, these granitoid clasts potentially suggest that the basement might be more heterogeneous than the highly comparable geochemical composition of the bulk of the intersected Hole M0077A core granitoids suggests.

Based on distinct geochemical markers, the dolerites reflect mantle-derived material with hints of partial hydration. The Th/Yb and Nb/Yb ratios indicate an enriched (E-MORB) source (Fig. 7; Pearce, 2014), and the linear relationships between HFSEs (Fig. 6) suggest the variations in the concentrations of these elements result from fractional crystallization. Interestingly, as opposed to the other pre-impact lithologies, there is an absence of pronounced Nb and Ta anomalies, and the trace-element pattern is flatter, less fractionated, but overall more enriched relative to CI-chondrite values (Fig. 5). These characteristics indicate the dolerites lack the pronounced continental arc signatures exhibited in the granitoids, and they show no definitive indication of being derived from normal (N-)MORB or E-MORB, as the former would show LREE-depleted signatures (e.g., Sun and McDonough, 1989), whereas the latter would show LREE-, Nb-, and Ta-enriched signatures (e.g., Gale et al., 2013). The higher Al_2O_3 content with increased differentiation (Fig. 4) indicates the retention of Al_2O_3 in the source and thus delayed fractionation of plagioclase. This relationship is a strong indication of hydration in the source region (Sisson and Grove, 1993). Based on the high MgO, flat MREE to HREE patterns, and slight negative Yb anomaly (Figs. 4 and 5B), we postulate this hydration thus resulted from interaction with dehydrating (depleted) mantle ultramafic rocks, either in the asthenospheric or lithospheric mantle. This interaction would indicate shallower fractionation of the source region, a feature much more prevalent at island arcs than at mid-ocean ridges or ocean islands (Pearce and Peate, 1995). Previous work interpreted these dolerites to be derived from ocean-island basalt (OIB) (Zhao et al., 2020); however, the aforementioned characteristics exclude OIBs, as these would show a more fractionated trace-element signature. Alternatively, based on the absence of a pronounced arc signature expected for typical island-arc environments (e.g., Elliott et al., 1997), we propose that these dolerites were sourced from enriched mantle material with an elemental signature most akin to a back-arc environment. Whether this implies the dolerites were formed in a back-arc environment or were sourced from a mantle source with ancient subducted material in the source region (similar to present-day Indian MORB source; Zhang

et al., 2005) requires more investigation and is outside the scope of this paper.

The felsites show distinct enrichment in most trace elements relative to the granitoids despite being trachyandesitic in composition (Figs. 4 and 5C). These felsites are characterized by the entrainment of partially digested granitoid clasts (Fig. 3), a feature the dacites and dolerites lack. This result indicates that these lithologies were hot enough during intrusion to partially melt the granitic host rock. Based on these features and the enriched nature of their trace elements, the felsites likely represent intracrustal partial melts of granitoid rock.

The dacites are geochemically comparable to the granitoids, but with slightly higher concentrations for all reported elements. These dacites only appear to strongly differ from the granitoids in texture and mineral assemblage. This difference indicates the dacites potentially originated from the same magmatic source as the granitoids but have undergone less fractional crystallization to account for the porphyritic texture (Fig. 3). However, without age constraints on these rocks, their geodynamic relation to the other basement lithologies remains elusive.

Lastly, the limestones most likely sample the carbonate target rock that covers the majority of the Yucatán Peninsula (Lopez Ramos, 1975). Apart from their anomalously high La, these samples fall within error of the carbonate end-member compositions of the Yax-1 impactites (Fig. 6) and, thus, can be interpreted as carbonate platform sediments incorporated into the Chicxulub impactites. Importantly, the granitoids, dolerites, and limestones reflect the most felsic, mafic, and CaO-rich lithologies sampled in the Hole M0077A core, respectively (Fig. 4; Appendix S1), whereas the felsites reflect the lithology most enriched in trace elements. For all reported major and trace elements, the compositional ranges of the majority of the upper impact melt rock unit and lower impact melt rock–bearing unit fall in between the values reported for the pre-impact lithologies, marking the pre-impact rocks identified and investigated in this study as the likely compositional end members of the impactites (Figs. 4 and 6–8).

Impact Melt Rock Compositions and Target Rock Contributions

The upper impact melt rock unit and the lower impact melt rock–bearing unit recovered from Hole M0077A are highly comparable in trace-element composition (Figs. 5E–5F), but distinct compositional variations are observed for most major elements (Fig. 4). Fractions of the impact melt have previously been suggested to have incorporated components of the carbonate tar-

get rock (e.g., Haiti yellow glass; Koeberl and Sigurdsson, 1992; Belza et al., 2015), which can explain major-element dilution. To ascertain the potential effects of carbonate dilution and explain the major-element differences seen between the upper impact melt rock unit and the lower impact melt rock–bearing unit, mixing lines recalculated on a CaO-free basis between the granitoids and dolerites were drawn (Fig. 9).

In Figure 9, both the upper impact melt rock unit and lower impact melt rock–bearing unit plot close to one another on a mixing line between granitoid and dolerite for FeO*, TiO_2, and MgO. However, we can observe that for Al_2O_3, only the lower impact melt rock–bearing unit plots on this mixing line, whereas the upper impact melt rock unit is offset from this line toward higher concentrations. As the bulk of the upper impact melt rock unit consists of quenched impact melt rock, the observed offset is likely the result of the low-temperature alteration of (originally vitric) melt to (alumina)phyllosilicates, as the latter are ubiquitous throughout the upper impact melt rock unit (see petrography; Fig. 3). This difference in Al_2O_3 content thus highlights the textural differences between the upper impact melt rock unit and the lower impact melt rock–bearing unit, with the upper impact melt rock unit dominated by vitric material and the lower impact melt rock–bearing unit dominated by basement-derived clasts, respectively.

Since the normalized data suggest that both the upper impact melt rock unit and the lower impact melt rock–bearing unit generally reflect the mixing of crystalline basement material (granitoid + dolerite), the differences in the nonnormalized major-element contents between both impactites likely result from variations in CaO content (cf. Figs. 4 and 9). Clasts of partially digested limestone occur in the upper impact melt rock unit (both on macroscopic and microscopic scale; Fig. 3A), whereas no limestone or other carbonate clasts have been observed in any of the lower impact melt rock–bearing unit dikes. These observations strongly indicate that the upper impact melt rock unit and the lower impact melt rock–bearing unit reflect impactites derived from impact melt rock formed through bimodal melting and mixing of felsic and mafic target rock components, but with the incorporation of carbonate material in one, but not in the other. This finding suggests that the incorporation of the carbonate platform target rock material only affected parts of the Chicxulub impact melt rock (as was previously demonstrated by Claeys et al., 2003; Tuchscherer et al., 2006; Belza et al., 2015), the implications of which are further discussed in the following sections.
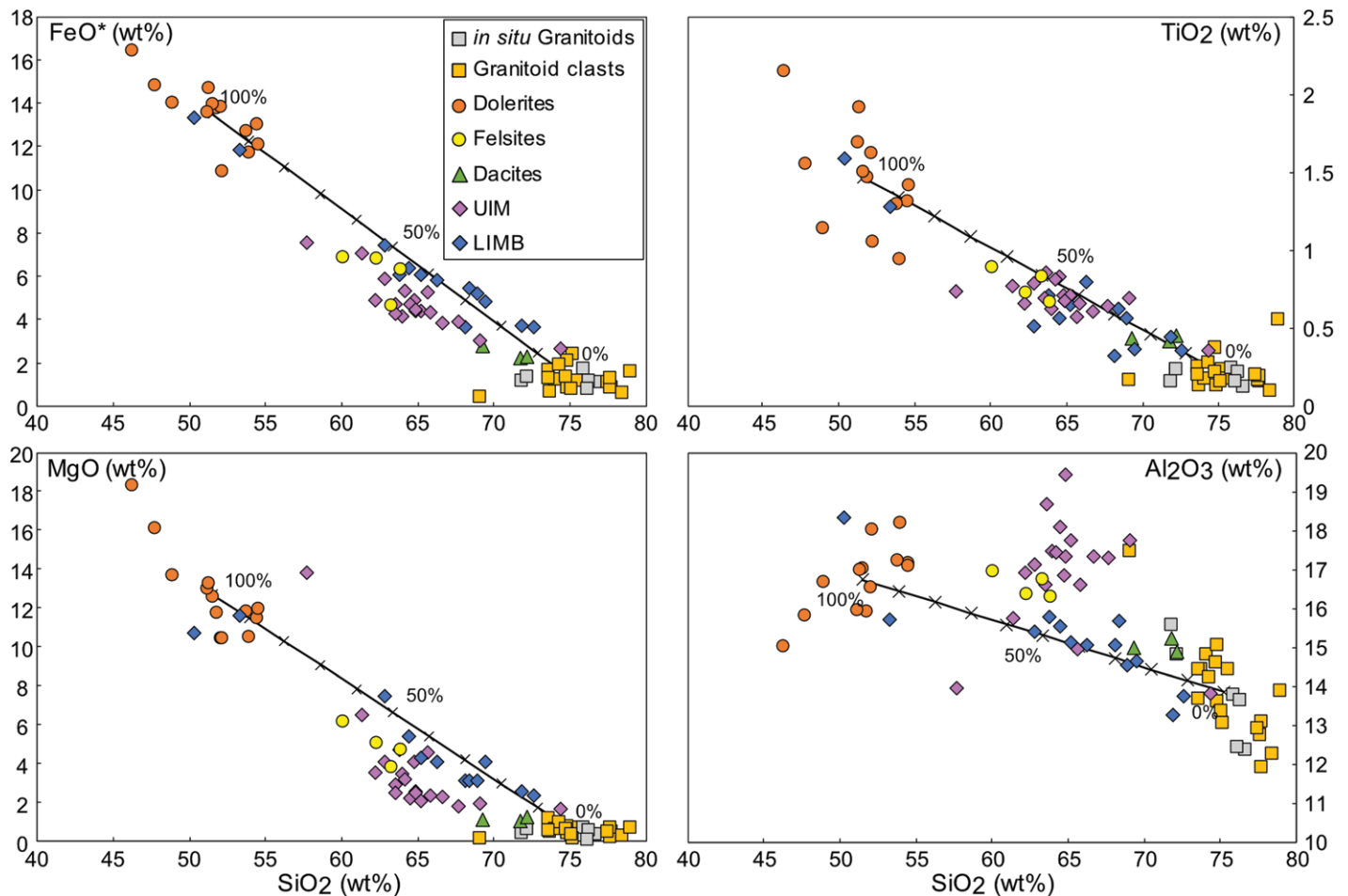
Figure 9. Major-element compositions of impactites and pre-impact lithologies with all lithologies recalculated on a CaO- and volatile-free basis. Mixing lines were calculated between averaged compositions of granitoid and dolerite. Each cross represents 10% mixing increments. UIM—upper impact melt rock unit; LIMB—lower impact melt rock–bearing unit.

To further refine the target rock contributions and differences between the upper impact melt rock unit and lower impact melt rock–bearing unit, the data were plotted on a CaO–K$_2$O + Na$_2$O–FeO* + MgO ternary diagram along with known bulk impact melt rock(-bearing) and impact melt particle compositions from previous studies (Fig. 10A). A distinct grouping of the impactites is observed: The lower impact melt rock–bearing unit falls between granitoid and dolerite and does not overlap with any other known composition; in contrast, the upper impact melt rock unit is offset from this intermediate composition toward higher CaO values, overlapping with three different melt compositions: C-1 melt rock, Y-6 melt breccia, and Haiti black glass ejecta. These observations demonstrate that the upper impact melt rock unit is part of the impactite suite sampled in other cores and ejecta (e.g., those presented in Claeys et al., 2003; Tuchscherer et al., 2006; Belza et al., 2015),

whereas the lower impact melt rock–bearing unit constitutes a distinctly different form of impact melt rock–bearing lithology. What is counterintuitive to this conclusion, however, is that the bulk trace-element compositions of the upper impact melt rock unit and lower impact melt rock–bearing unit are rather comparable, and both fall within error of known Chicxulub impact melt particle compositions for HFSEs (the siliceous end member of the Yax-1 impactites [SEMY]; Tuchscherer et al., 2005; Fig. 6). When averaging their compositions, these similarities are further emphasized (Fig. 10B). Yet, slight variations can be observed, with enrichment in Ba, Ce, and Sr occurring in the upper impact melt rock unit. While these elements are highly mobile and, like La, potentially reflect alteration, Ba, Ce, and Sr are trace elements available in the limestones sampled from the upper impact melt rock unit. As all other trace-element contents are comparatively low in the limestones, the aforementioned elemental com-

position might highlight the selective incorporation of carbonate target rock (i.e., limestone) in the upper impact melt rock unit when compared to the lower impact melt rock–bearing unit. This result illustrates that, for the most part, the trace-element patterns of the impactites are determined by the crystalline basement components.

To further substantiate this interpretation, the incorporation of the crystalline target rock components was examined by calculating mixing curves for La/Yb and SiO$_2$ compositions between the mafic dolerites and all other more felsic crystalline target rocks (Fig. 8C). The mixing curves show two things. First, binary mixing between averaged dolerite and felsite or dacite alone cannot explain the overall low La/Yb ratios of the upper impact melt rock unit and lower impact melt rock–bearing unit (Fig. 8C). This issue is further corroborated with the observation that the low La/Yb ratios of both impactites are determined
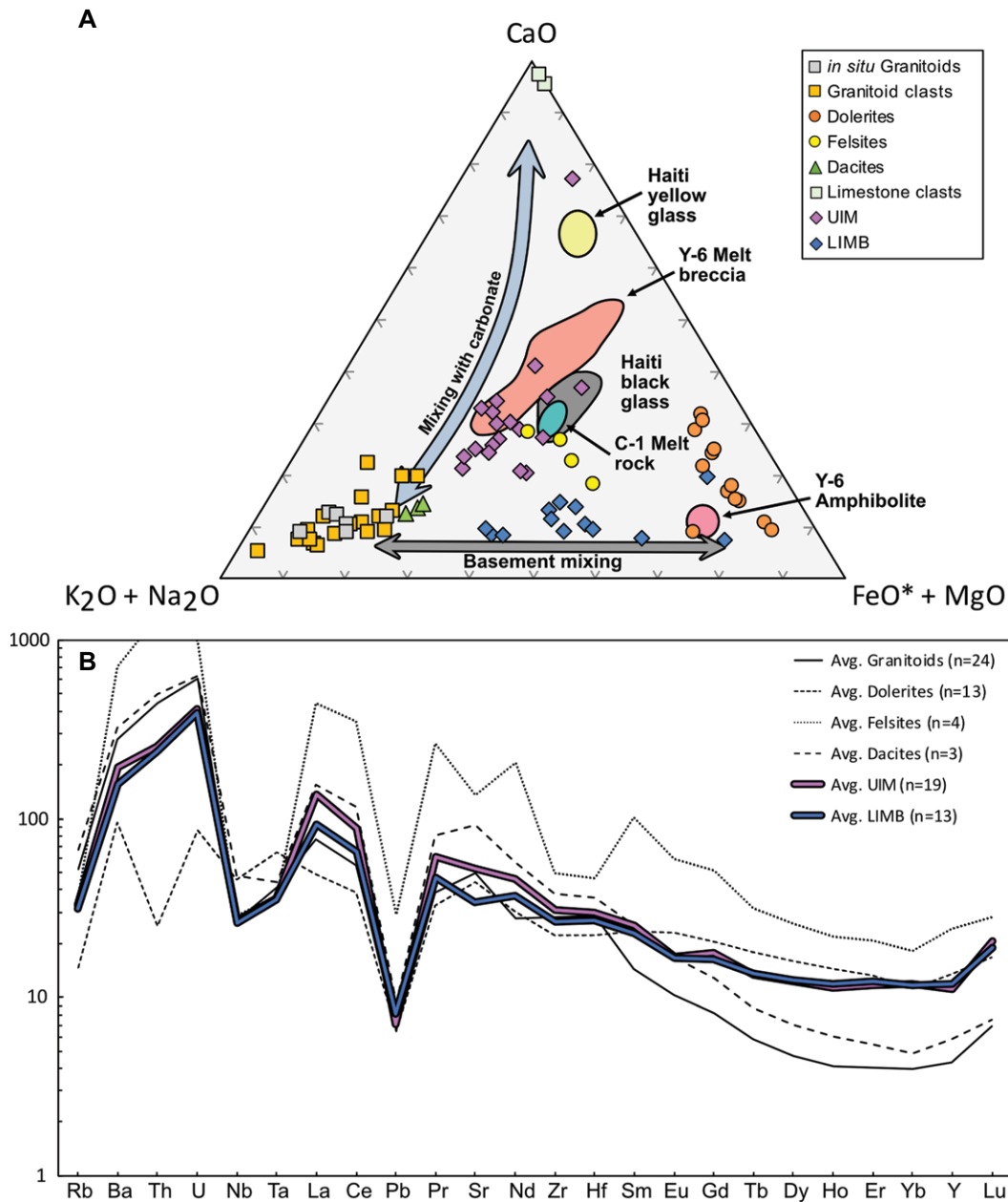
Figure 10. (A) Ternary CaO–K₂O + Na₂O–FeO* + MgO diagram (modified from Kettrup and Deutsch, 2003), with C-1 melt rock (Schuraytz et al., 1994; Kettrup and Deutsch, 2003), Y-6 melt breccias (Kettrup and Deutsch, 2003), and Haiti black and yellow glass fields (Koeberl and Sigurdsson, 1992). (B) Averaged compositions of CI-chondrite–normalized trace-element concentrations with normalization values from Sun and McDonough (1989). UIM—upper impact melt rock unit; LIMB—lower impact melt rock–bearing unit.

by high Yb over La content (Figs. 5 and 8B), precluding a significant role for the more LREE-enriched felsites or dacites. Second, the mixing curves calculated between dolerite and either granitoid constrain the compositions of both the upper impact melt rock unit and lower impact melt rock–bearing unit. This strongly implies that these lithologies represent the major components that contributed to the bulk of both impactite compositions. The remaining heterogeneity observed between samples and the slight offset from the mixing lines are likely due to imperfect mixing during impact processes such as vaporization, transport during crater modification, variations in

shock pressure and temperature (e.g., Hörz et al., 2002), as well as target heterogeneities (e.g., Kettrup et al., 2003). Examples are upper impact melt rock unit sample 95_3_55_57 and two lower impact melt rock–bearing unit samples (194_3_19_21 and 293_3_0_3). The upper impact melt rock unit sample shows a CI-chondrite–normalized pattern with distinct La, Ce, Pr, Nd, Sm, and Gd enrichments most comparable to the felsites (Fig. 5). This enrichment might be related to a localized input of the more enriched felsite lithology. The two lower impact melt rock–bearing unit samples consistently cluster close to doleritic major- and trace-element compositions, which

likely indicates the incorporation of a majority doleritic component (Figs. 4, 9, and 10; Appendix S1).

Alternatively, the lesser enrichment of the incompatible element Yb in the impactites provides an argument for impact melt differentiation. As the upper impact melt rock unit reflects the top portion of the entire impact melt rock layer of the Chicxulub impact structure, and thus was the first to quench, it would be comparatively more enriched in compatible elements (e.g., Yb and other HREEs). However, apart from the observed plagioclase and pyroxene microlites (Figs. 3A–3B), no other indications for significant differentiation are

observed in the Hole M0077A impact melt rocks. As such the low La/Yb ratios of both the upper impact melt rock unit and lower impact melt rock–bearing unit are not considered to be the result of differentiation but rather represent simple binary mixing between the mafic dolerite and felsic granitoid, with no further need for large-scale, complex, three-component mixing. Importantly, because the granitoids and dolerites explain the bulk of the impactite data, we thus conclude that the dolerites reflect the major mafic component incorporated into the impact melt.

Previous research has suggested that amphibolites reflect the mafic end member of the Chicxulub impact melt rock (Kettrup and Deutsch, 2003). However, while the amphibolites' mafic composition (Fig. 10A) does fit the required end-member composition, the sparseness of this lithology (Tuchscherer et al., 2005; this study) likely precludes them from being the major mafic component incorporated into the Chicxulub impactites, especially when compared to the pervasive dolerite dikes recovered in Hole M0077A. Following this reasoning, we postulate that the doleritic magmatic sequence extensively intruded large portions of the Yucatán basement.

In conclusion, the petrographic observations as well the normalized and nonnormalized geochemical data (Figs. 3, 4, 5, 9, and 10) presented here indicate that the upper impact melt rock unit represents a clast-bearing impact melt rock that incorporated carbonate rock and crystalline basement material of predominantly granitoid and dolerite compositions. This formed an andesitic composition with a distinct carbonate component strongly comparable to the impact melt rocks and impact melt particles sampled in other Chicxulub crater cores and ejecta (Fig. 10; Koeberl and Sigurdsson, 1992; Schuraytz et al., 1994; Kettrup and Deutsch, 2003; Tuchscherer et al., 2005). These observations likely hold true for the entire upper portion of the Chicxulub impact melt rock. The lower impact melt rock–bearing unit represents a brecciated impact melt rock (Figs. 3E–3G) that solely constitutes crystalline basement derived materials and displays a complete lack of a carbonate component. This finding marks the lower impact melt rock–bearing unit as a lithology that is different from the impact melt rocks and impact melt particles sampled in other drill cores, reflecting the greater depth of penetration into the basement and/or the peak ring setting of IODP-ICDP Site M0077. The variation between the upper impact melt rock unit and lower impact melt rock–bearing unit implies different formational processes and emplacement.

Impact Melt Rock Emplacement in the Peak Ring Structure

Different mechanisms have to be considered to explain the formation of impact melt rock with a carbonate component (upper impact melt rock unit) and a brecciated impact melt rock devoid of a carbonate component (lower impact melt rock–bearing unit) during peak ring formation. As the lower impact melt rock–bearing unit mainly constitutes crystalline basement material, a straightforward explanation is simply that it is the result of in situ frictional melting of crystalline target rock (as observed in pseudotachylites; e.g., Dressler and Reimold, 2004). However, the presence of "exotic" (i.e., nongranitoid) clasts in the lower impact melt rock–bearing unit and the observed intermediate geochemical composition preclude it from simply having formed by frictional melting of the surrounding granitoid basement (Riller et al., 2018; Kovaleva et al., 2020). These observations suggest significant mobility of the lower impact melt rock–bearing unit material. As such, the impact melt shards in the lower impact melt rock–bearing unit (Figs. 3E–3G) are interpreted as preserved quenched impact melt particles that were emplaced in the granitoid target rock, rather than having formed in situ.

In both the upper impact melt rock unit and lower impact melt rock–bearing unit, we observe two distinct types of melt particles, cryptocrystalline, dark-brown to black, and typically angular particles, and holohyaline, brown, and globule-like particles (Fig. 3). The cryptocrystalline particles are typically angular and must have cooled rapidly, whereas the holohyaline globules exhibit clear fluidal textures, indicating a (semi-)liquid state during deposition. Both melt particles occur in the Yax-1 core suevite unit (Tuchscherer et al., 2006). In Yax-1, the angular melt particles were interpreted as having cooled swiftly, deposited as quenched shard-like fragments and incorporated into groundmass. The angular morphology, vesiculation, and small sizes imply a volatile-rich and extremely turbulent environment prior to deposition (Tuchscherer et al., 2006). Conversely, the globule-like particles were interpreted to have been deposited in a semiplastic state as a result of the retention of latent heat (Tuchscherer et al., 2006). These melt particles are inherently similar to the ones observed in this study and imply melt injection quickly followed impact melt formation. Importantly, both types of impact melt clasts have been observed in other impactites of Hole M0077A (upper impact melt rock unit—this study, and suevite—e.g., Kaskes et al., 2019; Osinski et al., 2020). This pattern strongly suggests that initial impact melt rock injection into the granitoid basement occurred directly after impact melt

formation to account for the presence of the two types of melt particles in all impactites (including suevite).

Considering the timing of melt injection, multiple studies have demonstrated that as shock evaporation removed CaO-rich lithologies (carbonates and evaporites) from the center of the structure (e.g., Gulick et al., 2019) at the beginning of impact, CaO-rich material would not have reentered the crater until the modification and settling stage (Gulick et al., 2019; Osinski et al., 2020). Moreover, numerical modeling has shown a quick drop-off in shock pressures near the surface and outwards from the point of impact (Morgan et al., 2016; Artemieva et al., 2017), which can explain the preservation of CaO-rich material toward the crater rim. These studies demonstrate the possibility for either impact melt rock interaction with CaO-rich material away from the center of the crater and/ or the re-introduction of CaO-rich material at a later stage of crater formation. In either case, this would explain the lack of carbonate components in the impact melt rock in the center of the crater and constrains the timing of impact melt rock injection to the period after the initial formation of impact melt rock but before the introduction of a CaO-rich component.

In Yax-1 samples, Wittmann et al. (2004) described the injection of clastic polymict dike breccias with a predominance of host rock–derived clasts that formed during the excavation and crater modification stages. These dike breccias were interpreted to postdate the earliest formation of impact melt injection during the compression stage, whereas granular flow, likely during the modification stage, could have caused further comminution of the material (Wittmann et al., 2004). As the lower impact melt rock–bearing unit clearly shows the need for a mechanism to account for grain-size reduction (Figs. 3E–3G), the processes described by Wittmann et al. (2004) are able to explain this comminution and potentially constrain the reworking of the impact melt rock that would form the lower impact melt rock–bearing unit to a similar timing. Therefore, we suggest melt injection must have quickly followed impact melt formation, and further comminution of the lower impact melt rock–bearing unit initiated during the early stages of crater modification, at the latest during central uplift collapse.

Alternatively, Riller et al. (2018) constrained the bulk of impact melt emplacement in the lower impact melt rock–bearing unit to the end of peak ring formation (i.e., modification stage), based on the absence of shear faults in the melt rock of the lower impact melt rock–bearing unit. While their model is highly comparable to that suggested here, we note that in the lower impact

melt rock–bearing unit, globule-like melt particles, larger grains with melt coating, and an abundance of (now-altered) vitric material in the matrix can be observed (Figs. 3E–3G). These particles suggest that the lower impact melt rock–bearing unit contained viscous impact melt material during emplacement. Furthermore, the contacts between the lower impact melt rock–bearing unit and the granitoid can occur at very steep angles (close to 60° in cases), which are possible indications of friction melting during collapse of the central uplift (Reimold and Gibson, 2005). Whether or not these observations conclusively imply frictional melting during collapse of the central uplift and/or the emplacement of impact melt rock prior to central uplift collapse cannot be ascertained based on the limited spatial continuity that a single core provides. However, the presence of more viscous melt material could explain the propensity of ductile deformation over shear faulting and is able to reconcile the absence of shear faults observed by Riller et al. (2018). In both cases, the collapse and lateral movement of the central uplift would have effectively used the lower impact melt rock–bearing unit as a major delamination layer accommodating the movement during peak ring formation.

Following these assertions, we postulate the following model for the formation of the lower impact melt rock–bearing unit (Fig. 11): (1) Initial impact melt rock injection took place right after impact melt formation during the compression-excavation stage, specifically during the transient cavity formation (Fig. 11B), but potentially up until central uplift buildup (Fig. 11C). (2) The gravitational collapse of the central uplift and the subsequent lateral movement of the basement material directly afterward (Morgan et al., 2016; Riller et al., 2018) likely further fragmented, brecciated, and potentially (re)melted the material (Fig. 11D). Following the observation that the lower impact melt rock–bearing unit is documented at multiple intervals throughout the Hole M0077A core, it stands to reason that more material like the lower impact melt rock–bearing unit is present throughout the peak ring structure (Fig. 11E), which may have been important as slip surfaces during peak ring emplacement (e.g., Riller et al., 2018). The thickest of these melt-related structures may form seismic reflectors within the peak ring (fig. 1G *in* Morgan et al., 2016). Following these interpretations, the lower impact melt rock–bearing unit likely acted as a delamination layer within the granitoid, accommodating the movement of the granitoid outwards during peak ring formation. This process would be similar to that described in Riller et al. (2018) for the thickest lower impact melt rock–bearing interval near the base of Hole M0077A and comparable to that of strongly localized granular flow accommodating mass movement during the crater modification stage (Melosh, 1983).

Lastly, in the model presented in Figure 11, we need to reconcile the formation of the upper impact melt rock unit. In the initial stages, most carbonate material was ejected and vaporized from the crater center (Artemieva et al., 2017; Gulick et al., 2019), while the impact melt rock that would form the upper impact melt rock unit stayed at the surface during crater evolution. From the presence of small plagioclase and pyroxene microlites and preserved limestone material in the impact melt rock (Figs. 3A–3C), we need to explain a temperature range at which these phases can fractionate yet limestone material is preserved. Engelhardt et al. (1995) determined that plagioclase microlites can crystallize from ~750 °C at 10 bar water pressure down to ~550 °C at 600 bar water pressure. Moreover, they determined that at ~650 °C and water pressure between 20 and 50 bar, plagioclase and pyroxene crystallize without biotite. As biotite is not observed as phenocrysts in the upper impact melt rock unit (Fig. 3), this determination potentially constrains the temperature ranges in the upper impact melt rock unit to have been between ~650 °C and 750 °C. This temperature range is well below the minimum decomposition temperature of limestone (i.e., Ca-rich carbonate; ~825 °C) (Oates, 1998) and can thus reconcile the incorporation and preservation of Ca-rich carbonate target rock into the impact melt rock with the formation of both plagioclase and pyroxene microlites.

The schlieren observed in the upper subunit of the lower impact melt rock–bearing unit could, therefore, represent carbonate target rock that melted in contact with impact melt rock, forming a lithology comparable to a carbonatite. Notably, the green schlieren sampled in the upper impact melt rock unit plot close to Haiti yellow glass ejecta (Fig. 10A), which is interpreted to have incorporated the carbonate target rock (Belza et al., 2015). This form of CaO-rich melt rock would likely not be able to fully mix with the SiO_2-rich black melt rock of the upper impact melt rock unit unless the pressure and temperature were sufficiently high (Claeys et al., 2003), owing to their compositional differences, thus forming the mingling textures that we can observe in the core (Fig. 2). Other studies (e.g., Osinski et al., 2020) interpreted the green schlieren to be the product of massive brecciation as a result of melt–water interaction with subsequent calcite precipitation in the cracks. While this works for the upper portion of the upper impact melt rock unit, this does not explain the mingling textures toward the base of Unit 3a (Fig. 2). Moreover, at the transition between Units 3a and 3b, green schlieren disappear from the unit, yet a similar CaO content to the upper unit is observed here (Fig. 4), strongly indicating that mixing between siliceous melt and carbonate material did indeed occur.

We propose that the upper part of the upper impact melt rock unit is characterized by the melt–water interaction as already described by Gulick et al. (2019) and Osinski et al. (2020), but the lower portion of Unit 3 documents the mingling and mixing of SiO_2- and CaO-rich melts. This transition from mixing to mingling to brecciation from the bottom toward the top of the upper impact melt rock unit reflects a difference in latent heat, allowing for assimilation of carbonate in one part and mingling in the other part. This observation highlights that incorporation of the CaO-rich component had to have happened when the melt was still hot, before quenching of the material as a result of resurging water. With the knowledge that water did not reenter the crater until tens of minutes after formation (Gulick et al., 2019), this stratigraphic variation in the upper impact melt rock unit shows that SiO_2- and CaO-rich melts interacted in the early stages of crater formation, in the first few minutes (Fig. 11; Morgan et al., 2016; Riller et al., 2018; Gulick et al., 2019), which postdated the initial lower impact melt rock–bearing unit injection and peak ring formation. Importantly, this sequence makes the model suggested here compatible with numerical and observational studies on the Chicxulub impact structure formation (e.g., Morgan et al., 2016; Riller et al., 2018; Gulick et al., 2019). Lastly, the observation that isolated impact melt particles and ejecta are more heterogeneous than the bulk of the impactite data presented here (e.g., Kettrup and Deutsch, 2003; Tuchscherer et al., 2006; Belza et al., 2015) likely resulted from volatilization prior to homogenization, which is reflected in the wide compositional variety of Chicxulub impact ejecta (Koeberl and Sigurdsson, 1992; Smit et al., 1992; Alvarez et al., 1992; Bohor and Glass, 1995; Belza et al., 2015). Following the initial volatilization, the redistribution and mixing of impact melt during crater formation subsequently homogenized the bulk compositions of Chicxulub impactites (Fig. 10B).

CONCLUSIONS

The IODP-ICDP Expedition 364 Hole M0077A impactites and pre-impact basement lithologies presented in this study provide new insights into the formation of the Chicxulub impact structure, impact melt rock formation, and Yucatán basement composition. The geochemical
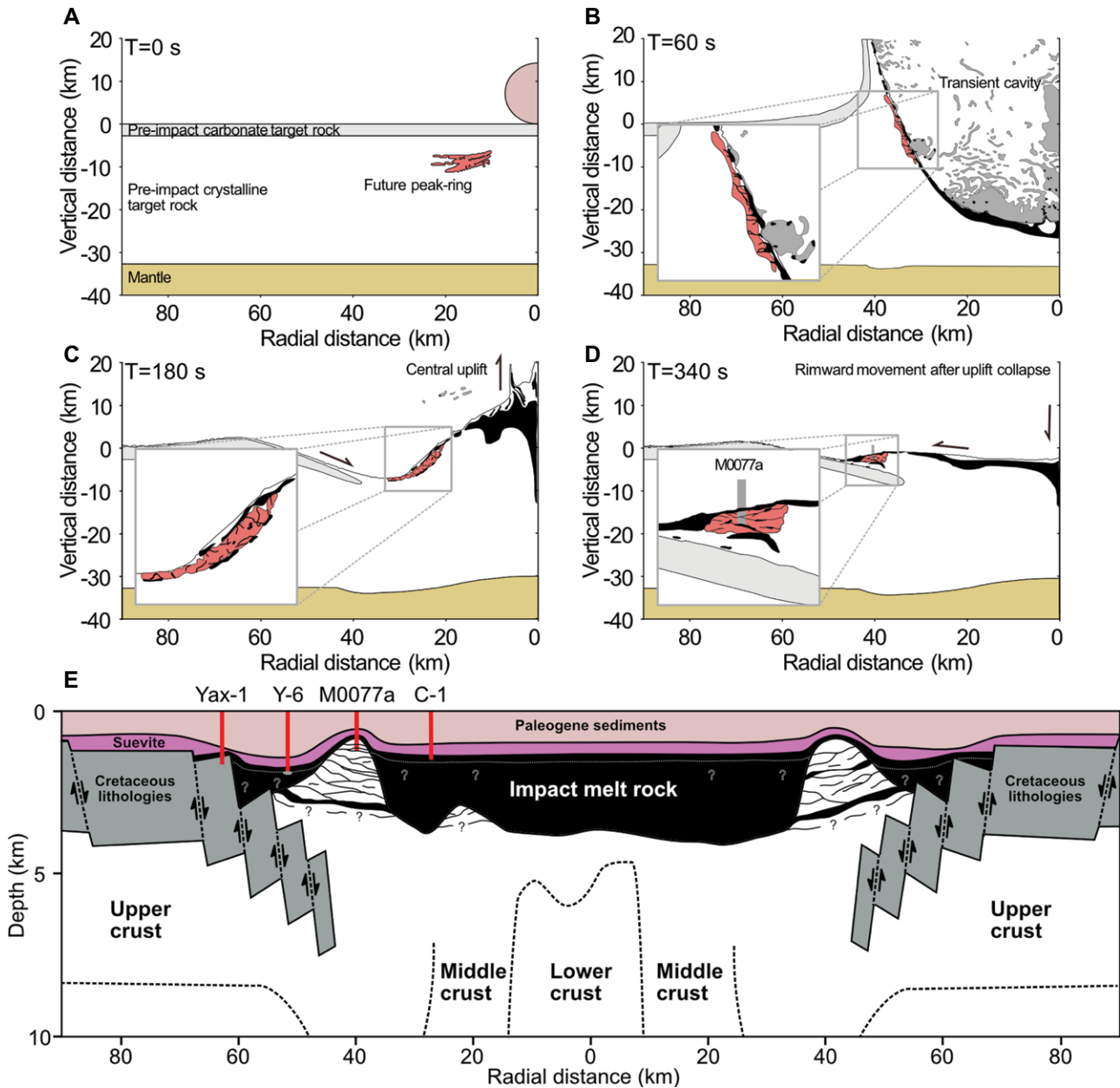
Figure 11. Model of peak ring formation, adapted from Morgan et al. (2016) and Riller et al. (2018). Black areas represent impact melt rock after Morgan et al. (2016); black lines in future peak ring granitoid represent intruded impact melt rock. Insets show a zoomed-in view of the future peak ring granitoid. (A) Simplified undisturbed cross section and starting conditions before impact. (B) Transient cavity is formed, and future peak ring moves up and outward. Majority of impact melt rock formed as a result of shock melting is located in the center of the crater. Part of the impact melt rock intrudes the future peak ring at this stage and becomes isolated from the majority of the melt sheet. Ejected pre-impact material is shown in gray. (C) As the excavation energy of the impact dissipates, the transient cavity collapses, and lithospheric rebound causes central uplift. The future peak ring moves inward and up. Impact melt rock is at this stage well emplaced within the granitoid. (D) After central uplift collapse, the future peak ring moves down and rimward. While accommodating movement of the granitoid, the intruded impact melt rock is reworked to the lower impact melt rock–bearing unit. Upper impact melt rock now overlies the granitoid. (E) Simplified cross section with vertical exaggeration of the final Chicxulub crater, with important drilling campaigns highlighted, modified after Claeys (2006) and Vermeesch and Morgan (2008). Yax-1—Yaxcopoil-1; Y-6—Yucatán-6; C-1—Chicxulub-1; M0077A—International Ocean Discovery Program (IODP) and International Continental Scientific Drilling Program (ICDP) Expedition 364 Hole M0077A. Y-6 sampled a dolo-anhydrite breccia at the base, indicating the potential lower boundary of "upper impact melt rock unit [UIM]–type impact melt rock" in the annular trough of the crater; as such, the gray dotted line represents the extrapolated thickness of UIM-type melt rock throughout the crater. Note that the extent of lower impact melt rock–bearing unit dikes in the peak ring below the Hole M0077A core is exaggerated to illustrate the point; it is not based on seismic data.

compositions of the pre-impact lithologies encompass those of the impactites and, thus, represent the principal components contributing to their formation. The impactites display an andesitic composition formed from the melting and mixing of primarily granitoid and dolerite crystalline target rock compositions, with varying degrees of carbonate target rock admixture. This strongly suggests that the dolerites sampled here represent the ubiquitous mafic component that contributed to the impact melt rocks recovered throughout the Chicxulub impact structure, rather than the previously suggested, relatively rare, amphibolite. Consequently, the pre-impact lithologies sampled in the Hole M0077A core are likely widespread throughout the northern Yucatán subsurface and, thus, played an important role during the tectonic history of the Maya block.

Based on petrography and geochemistry, the impactites presented here can be subdivided into two distinct units: the lower impact melt rock–bearing unit and the upper impact melt rock unit. Both units formed from the same impact melt but diverged during crater formation. The lower impact melt rock–bearing unit is broadly characterized as a brecciated impact melt rock that shows no indication of carbonate dilution, while the upper impact melt rock unit is characterized as a clast-bearing impact melt rock with a distinct carbonate component. The lower impact melt rock–bearing unit is interpreted to initially have been injected as impact melt into the crystalline target rock during the compression-excavation stage and/or no later than the beginning of the modification stage of crater formation. Further modification (i.e., brecciation) of the lower impact melt rock–bearing unit occurred after central uplift collapse. This impact melt rock layer likely acted as (one of many) delamination layers within the granitoid and accommodated the movement of the granitoid blocks during peak ring formation. The lack of carbonate in this unit is explained by the carbonate target rock being initially largely ejected and vaporized from the crater during the compression stage. The upper impact melt rock unit stayed at the surface during crater development, and, to account for the entrainment of nonvaporized carbonate target rock, we suggest that its formation was not finalized until the modification and water resurge stages, when the bulk of the carbonate material would have reentered the crater.

The recognition that the compositions of impact melt rock, impact melt rock particles, and ejecta from other drill cores are mostly comparable to the upper impact melt rock unit, whereas the lower impact melt rock–bearing unit has so far only been sampled in the Hole M0077A core, represents an important observa-

tion. When compared to the size of the crater ($\sim$200 km), the upper impact melt rock unit only constitutes a relatively minor thickness ($\sim$26 m), while the lower impact melt rock–bearing unit is volumetrically much more pervasive (exposed between 1206.98 and 1334.69 mbsf). This thickness, paired with the distinct geochemical differences between both impactite units, implies that the majority of impact melt rock sampled in other drill cores and ejecta only samples the top portion of the impact melt rock. The upper impact melt rock unit, and likewise all material sampled in other cores and ejecta, thus only constitutes the top layer of Chicxulub impact melt rock. This finding, paired with the volume of lower impact melt rock–bearing unit intersected in Hole M0077A, indicates that the bulk of the Chicxulub impact melt is likely more comparable to the lower impact melt rock–bearing unit, and thus was formed from a largely crystalline target rock composition.

ACKNOWLEDGMENTS

REFERENCES CITED

Abramov, O., and Kring, D.A., 2007, Numerical modeling of impact-induced hydrothermal activity at the Chicxulub crater: Meteoritics & Planetary Science, v. 42,
p. 93–112, https://doi.org/10.1111/j.1945-5100.2007.tb00220.x.

Alaniz-Álvarez, S.A., van der Heyden, P., Nieto-Samaniego, A.F., and Ortega-Gutiérrez, F., 1996, Radiometric and kinematic evidence for Middle Jurassic strike-slip faulting in southern Mexico related to the opening of the Gulf of Mexico: Geology, v. 24, no. 5, p. 443–446, https://doi.org/10.1130/0091-7613(1996)024<0443:RAKEFM>2.3.CO;2.

Alvarez, W., Smit, J., Lowrie, W., Asaro, F., Margolis, S.V., Claeys, Ph., Kastner, M., and Hildebrand, A.R., 1992, Proximal impact deposits at the Cretaceous-Tertiary boundary in the Gulf of Mexico: A restudy of DSDP Leg 77 Sites 536 and 540: Geology, v. 20, no. 8, p. 697–700, https://doi.org/10.1130/0091-7613(1992)020<0697:PIDATC>2.3.CO;2.

Ames, D.E., Kjarsgaard, I.M., Pope, K.O., Dressler, B., and Pilkington, M., 2004, Secondary alteration of the impactite and mineralization in the basal Tertiary sequence, Yaxcopoil-1, Chicxulub impact crater, Mexico: Meteoritics & Planetary Science, v. 39, no. 7, p. 1145–1167, https://doi.org/10.1111/j.1945-5100.2004.tb01134.x.

Artemieva, N., Morgan, J.V., and the Expedition 364 Science Party, 2017, Quantifying the release of climate-active gases by large meteorite impacts with a case study of Chicxulub: Geophysical Research Letters, v. 44, no. 20, p. 10180–10188, https://doi.org/10.1002/2017GL074879.

Belza, J., Goderis, S., Keppens, E., Vanhaecke, F., and Claeys, Ph., 2012, An emplacement mechanism for the mega-block zone within the Chicxulub crater (Yucatán, Mexico) based on chemostratigraphy: Meteoritics & Planetary Science, v. 47, no. 3, p. 400–413, https://doi.org/10.1111/j.1945-5100.2012.01345.x.

Belza, J., Goderis, S., Smit, J., Vanhaecke, F., Baert, K., Terryn, H., and Claeys, Ph., 2015, High spatial resolution geochemistry and textural characteristics of 'microtektite' glass spherules in proximal Cretaceous–Paleogene sections: Insights into glass alteration patterns and precursor melt lithologies: Geochimica et Cosmochimica Acta, v. 152, p. 1–38, https://doi.org/10.1016/j.gca.2014.12.013.

Bohor, B.F., and Glass, B.P., 1995, Origin and diagenesis of K/T impact spherules—From Haiti to Wyoming and beyond: Meteoritics, v. 30, no. 2, p. 182–198, https://doi.org/10.1111/j.1945-5100.1995.tb01113.x.

Claeys, Ph., 2006, Chicxulub, anatomy of a large impact structure: From impactite to ejecta distribution, *in* Proceedings of the 40th ESLAB Symposium "First International Conference on Impact Cratering in the Solar System": European Space Agency, European Space and Technology Centre, p. 81–92.

Claeys, Ph., Heuschkel, S., Lounejeva-Baturina, E., Sanchez-Rubio, G., and Stöffler, D., 2003, The suevite of drill hole Yucatàn 6 in the Chicxulub impact crater: Meteoritics & Planetary Science, v. 38, no. 9, p. 1299–1317, https://doi.org/10.1111/j.1945-5100.2003.tb00315.x.

Collins, G.S., Patel, N., Davison, T.M., Rae, A.S.P., Morgan, J.V., Fulick, S.P.S. IODP-ICDP Expedition 364 Science Party, and Third-Party Scientists, 2020, A steeply-inclined trajectory for the Chicxulub impact: Nature Communications, v. 11, p. 1480, https://doi.org/10.1038/s41467-020-15269-x.

Dengo, G., 1969, Problems of tectonic relations between Central America and the Caribbean: Transactions of the Gulf Coast Association of Geological Societies, v. 19, p. 311–320.

Donnelly, T.W., Horne, G.S., Finch, R.C., and López-Ramos, E., 1990, Northern Central America; the Maya and Chortis blocks, *in* Dengo, G., and Case, J.E., eds., The Caribbean Region: Boulder, Colorado, Geological Society of America, The Geology of North America v. H, p. 371–396, https://doi.org/10.1130/DNAG-GNA-H.37.

Dressler, B.O., and Reimold, W.U., 2004, Order or chaos? Origin and mode of emplacement of breccias in floors of large impact structures: Earth-Science Reviews, v. 67, no. 1–2, p. 1–54, https://doi.org/10.1016/j.earscirev.2004.01.007.

Elliott, T., Plank, T., Zindler, A., White, W., and Bourdon, B., 1997, Element transport from slab to volcanic front at the Mariana arc: Journal of Geophysical

Research–Solid Earth, v. 102, no. B7, p. 14991–15019, https://doi.org/10.1029/97JB00788.

Engelhardt, W.V., Arndt, J., Fecker, B., and Pankau, H.G., 1995, Suevite breccia from the Ries crater, Germany: Origin, cooling history and devitrification of impact glasses: Meteoritics, v. 30, no. 3, p. 279–293, https://doi.org/10.1111/j.1945-5100.1995.tb01126.x.

Feignon, J.-G., Ferrière, L., Leroux, H., and Koeberl, C., 2020, Characterization of shocked quartz grains from Chicxulub peak ring granites and shock pressure estimates: Meteoritics & Planetary Science, v. 55, p. 2206–2223, https://doi.org/10.1111/maps.13570.

Gale, A., Dalton, C.A., Langmuir, C.H., Su, Y., and Schilling, J.G., 2013, The mean composition of ocean ridge basalts: Geochemistry Geophysics Geosystems, v. 14, no. 3, p. 489–518, https://doi.org/10.1029/2012GC004334.

Goderis, S., Tagle, R., Belza, J., Smit, J., Montanari, A., Vanhaecke, F., Erzinger, J., and Claeys, Ph., 2013, Reevaluation of siderophile element abundances and ratios across the Cretaceous-Paleogene (K-Pg) boundary: Implications for the nature of the projectile: Geochimica et Cosmochimica Acta, v. 120, p. 417–446, https://doi.org/10.1016/j.gca.2013.06.010.

Gulick, S.P.S., Barton, P.J., Christeson, G.L., Morgan, J.V., McDonald, M., Mendoza-Cervantes, K., Pearson, Z.F., Surendra, A., Urrutia-Fucugauchi, J., Vermeesch, P.M., and Warner, M.R., 2008, Importance of pre-impact crustal structure for the asymmetry of the Chicxulub impact crater: Nature Geoscience, v. 1, p. 131–135, https://doi.org/10.1038/ngeo103.

Gulick, S.P.S., Morgan, J.V., Mellett, C.L., et al., 2017a, Site M0077: Upper peak ring, in Morgan, J.V., Gulick, S.P.S., Mellett, C.L., Green, S.L., and the Expedition 364 Scientists, Chicxulub: Drilling the K-Pg Impact Crater; Proceedings of the International Ocean Discovery Program, Volume 364: College Station, Texas, International Ocean Discovery Program, https://doi.org/10.14379/iodp.proc.364.106.2017.

Gulick, S.P.S., Morgan, J.V., Mellett, C.L., et al., 2017b, Site M0077: Lower peak ring, in Morgan, J.V., Gulick, S.P.S., Mellett, C.L., Green, S.L., and the Expedition 364 Scientists, Chicxulub: Drilling the K-Pg Impact Crater; Proceedings of the International Ocean Discovery Program, Volume 364: College Station, Texas, International Ocean Discovery Program, https://doi.org/10.14379/iodp.proc.364.107.2017.

Gulick, S.P.S., Bralower, T.J., Ormö, J., et al., 2019, The first day of the Cenozoic: Proceedings of the National Academy of Sciences of the United States of America, v. 116, no. 39, p. 19342–19351, https://doi.org/10.1073/pnas.1909479116.

Hecht, L., Wittmann, A., Schmitt, R.-T., and Stöffler, D., 2004, Composition of impact melt particles and the effects of post-impact alteration in suevitic rocks at the Yaxcopoil-1 drill core, Chicxulub crater, Mexico: Meteoritics & Planetary Science, v. 39, no. 7, p. 1169–1186, https://doi.org/10.1111/j.1945-5100.2004.tb01135.x.

Hildebrand, A.R., Penfield, G.T., Kring, D.A., Pilkington, M., Camargo, Z.A., Jacobsen, S.B., and Boynton, W.V., 1991, Chicxulub crater: A possible Cretaceous/Tertiary boundary impact crater on the Yucatán Peninsula, Mexico: Geology, v. 19, no. 9, p. 867–871, https://doi.org/10.1130/0091-7613(1991)019<0867:CCAPCT>2.3.CO;2.

Hörz, F., Mittlefehldt, D.W., See, T.H., and Galindo, C., 2002, Petrographic studies of the impact melts from Meteor Crater, Arizona, USA: Meteoritics & Planetary Science, v. 37, no. 4, p. 501–531, https://doi.org/10.1111/j.1945-5100.2002.tb00836.x.

Kamo, S.L., and Krogh, T.E., 1995, Chicxulub crater source for shocked zircon crystals from the Cretaceous-Tertiary boundary layer, Saskatchewan: Evidence from new U-Pb data: Geology, v. 23, no. 3, p. 281–284, https://doi.org/10.1130/0091-7613(1995)023<0281:CCSFSZ>2.3.CO;2.

Kamo, S.L., Lana, C., and Morgan, J.V., 2011, U-Pb ages of shocked zircon grains link distal K-Pg boundary sites in Spain and Italy with the Chicxulub impact: Earth and Planetary Science Letters, v. 310, no. 3–4, p. 401–408, https://doi.org/10.1016/j.epsl.2011.08.031.

Kaskes, P., de Graaff, S.J., Déhais, T., Goderis, S., Feignon, J.-G., Ferrière, L., Koeberl, C., Smit, J., and Claeys, Ph.,

2019, Geochemical and petrographic characterization of the suevite sequence within the IODP-ICDP Exp. 364 core of the Chicxulub peak ring, in Large Meteorite Impacts and Planetary Evolution VI: Lunar and Planetary Institute Contribution 2136, abstract 5085.

Keppie, J.D., Dostal, J., Norman, M., Urrutia-Fucugauchi, J., and Grajales-Nishimura, M., 2011, Study of melt and a clast of 546 Ma magmatic arc rocks in the 65 Ma Chicxulub bolide breccia, northern Maya block, Mexico: Western limit of Ediacaran arc peripheral to northern Gondwana: International Geology Review, v. 53, no. 10, p. 1180–1193, https://doi.org/10.1080/00206810903545527.

Kettrup, B., and Deutsch, A., 2003, Geochemical variability of the Yucatàn basement: Constraints from crystalline clasts in Chicxulub impactites: Meteoritics & Planetary Science, v. 38, no. 7, p. 1079–1092, https://doi.org/10.1111/j.1945-5100.2003.tb00299.x.

Kettrup, B., Deutsch, A., Ostermann, M., and Agrinier, P., 2000, Chicxulub impactites: Geochemical clues to the precursor rocks: Meteoritics & Planetary Science, v. 35, no. 6, p. 1229–1238, https://doi.org/10.1111/j.1945-5100.2000.tb01511.x.

Kettrup, B., Deutsch, A., and Masaitis, V.L., 2003, Homogeneous impact melts produced by a heterogeneous target?: Sr-Nd isotopic evidence from the Popigai crater, Russia: Geochimica et Cosmochimica Acta, v. 67, no. 4, p. 733–750, https://doi.org/10.1016/S0016-7037(02)01143-2.

Koeberl, C., 1993, Chicxulub crater, Yucatán: Tektites, impact glasses, and the geochemistry of target rocks and breccias: Geology, v. 21, no. 3, p. 211–214, https://doi.org/10.1130/0091-7613(1993)021<0211:CCYTIG>2.3.CO;2.

Koeberl, C., and Sigurdsson, H., 1992, Geochemistry of impact glasses from the K/T boundary in Haiti: Relation to smectites and a new type of glass: Geochimica et Cosmochimica Acta, v. 56, no. 5, p. 2113–2129, https://doi.org/10.1016/0016-7037(92)90333-E.

Kovaleva, E., Huber, M.S., and Dixon, R., 2020, Material mixing in shock-induced pseudotachylites, Vredefort impact structure, South Africa: Lithos, v. 370–371, p. 105621, https://doi.org/10.1016/j.lithos.2020.105621.

Kring, D.A., 2005, Hypervelocity collisions into continental crust composed of sediments and an underlying crystalline basement: Comparing the Ries (∼24 km) and Chicxulub (∼180 km) impact craters: Geochemistry, v. 65, no. 1, p. 1–46, https://doi.org/10.1016/j.chemer.2004.10.003.

Kring, D.A., and Boynton, W.V., 1992, Petrogenesis of an augite-bearing melt rock in the Chicxulub structure and its relationship to K/T impact spherules in Haiti: Nature, v. 358, p. 141–144, https://doi.org/10.1038/358141a0.

Kring, D.A., Hörz, F., Zurcher, L., and Urrutia-Fucugauchi, J., 2004, Impact lithologies and their emplacement in the Chicxulub impact crater: Initial results from the Chicxulub Scientific Drilling Project, Yaxcopoil, Mexico: Meteoritics & Planetary Science, v. 39, no. 6, p. 879–897, https://doi.org/10.1111/j.1945-5100.2004.tb00936.x.

Kring, D.A., Tikoo, S.M., Schmieder, M., et al., 2020, Probing the hydrothermal system of the Chicxulub impact crater: Science Advances, v. 6, no. 22, p. eaaz3053, https://doi.org/10.1126/sciadv.aaz3053.

Krogh, T.E., Kamo, S.L., Sharpton, V.L., Marin, L.E., and Hildebrand, A.R., 1993, U-Pb ages of single shocked zircons linking distal K/T ejecta to the Chicxulub crater: Nature, v. 366, p. 731–734, https://doi.org/10.1038/366731a0.

Langmuir, C.H., Klein, E.M., and Plank, T., 1992, Petrological systematics of mid-ocean ridge basalts: Constraints on melt generation beneath ocean ridges, in Morgan, J.P., Blackman, D.K., and Sinton, J.M., eds., Mantle Flow and Melt Generation at Mid-Ocean Ridges: American Geophysical Union Geophysical Monograph 71, p. 183–280, https://doi.org/10.1029/GM071p0183.

Le Maitre, R.W., Streckeisen, A., Zanettin, B., Le Bas, M.J., Bonin, B., and Bateman, P., eds., 2005, Igneous Rocks: A Classification and Glossary of Terms: Recommendations of the International Union of Geological Sciences Subcommission on the Systematics of Igneous Rocks (2nd ed.): Cambridge, New York, Cambridge University Press, 256 p.

Lopez Ramos, E., 1975, Geological summary of the Yucatán Peninsula, in Nairn, A.E.M., and Stehli, F.G., eds., The Gulf of Mexico and the Caribbean: Boston, Massachusetts, Springer, p. 257–282, https://doi.org/10.1007/978-1-4684-8535-6_7.

Melosh, H.J., 1983, Acoustic fluidization: Can sound waves explain why dry rock debris appears to flow like a fluid in some energetic geologic events?: American Scientist, v. 71, no. 2, p. 158–165.

Middlemost, E.A.K., 1994, Naming materials in the magma/igneous rock system: Earth-Science Reviews, v. 37, no. 3–4, p. 215–224, https://doi.org/10.1016/0012-8252(94)90029-9.

Molina-Garza, R.S., Van der Voo, R., and Urrutia-Fucugauchi, J., 1992, Paleomagnetism of the Chiapas Massif, southern Mexico: Evidence for rotation of the Maya block and implications for the opening of the Gulf of Mexico: Geological Society of America Bulletin, v. 104, no. 9, p. 1156–1168, https://doi.org/10.1130/0016-7606(1992)104<1156:POTCMS>2.3.CO;2.

Morgan, J.V., Warner, M., Chicxulub Working Group, et al., 1997, Size and morphology of the Chicxulub impact crater: Nature, v. 390, p. 472–476, https://doi.org/10.1038/37291.

Morgan, J.V., Gulick, S.P.S., Bralower, T., et al., 2016, The formation of peak rings in large impact craters: Science, v. 354, no. 6314, p. 878–882, https://doi.org/10.1126/science.aah6561.

Morgan, J.V., Gulick, S.P.S., Mellett, C.L., et al., 2017, Chicxulub: Drilling the K-Pg Impact Crater: Proceedings of the International Ocean Discovery Program, Volume 364: College Station, Texas, International Ocean Discovery Program, https://doi.org/10.14379/iodp.proc.364.2017.

Novak, G.A., and Gibbs, G.V., 1971, The crystal chemistry of the silicate garnets: The American Mineralogist, v. 56, no. 5–6, p. 791–825.

Oates, J.A., 1998, Lime and Limestone: Chemistry and Technology, Production and Uses: Weinheim, Germany, Wiley-VCH, 454 p., https://doi.org/10.1002/9783527612024.

Ortéga-Gutiérrez, F., Elías-Herrera, M., Morán-Zenteno, D.J., Solari, L., Weber, B., and Luna-González, L., 2018, The pre-Mesozoic metamorphic basement of Mexico, 1.5 billion years of crustal evolution: Earth-Science Reviews, v. 183, p. 2–37, https://doi.org/10.1016/j.earscirev.2018.03.006.

Osinski, G.R., Grieve, R.A.F., Hill, P.J.A., et al., 2020, Explosive interaction of impact melt and seawater following the Chicxulub impact event: Geology, v. 48, no. 2, p. 108–112, https://doi.org/10.1130/G46783.1.

Pearce, J.A., 2008, Geochemical fingerprinting of oceanic basalts with applications to ophiolite classification and the search for Archean oceanic crust: Lithos, v. 100, no. 1–4, p. 14–48, https://doi.org/10.1016/j.lithos.2007.06.016.

Pearce, J.A., 2014, Immobile element fingerprinting of ophiolites: Elements, v. 10, no. 2, p. 101–108, https://doi.org/10.2113/gselements.10.2.101.

Pearce, J.A., and Peate, D.W., 1995, Tectonic implications of the composition of volcanic arc magmas: Annual Review of Earth and Planetary Sciences, v. 23, p. 251–285, https://doi.org/10.1146/annurev.ea.23.050195.001343.

Pearce, J.A., Harris, N.B.W., and Tindle, A.G., 1984, Trace element discrimination diagrams for the tectonic interpretation of granitic rocks: Journal of Petrology, v. 25, no. 4, p. 956–983, https://doi.org/10.1093/petrology/25.4.956.

Quitté, G., Robin, E., Levasseur, S., Capmas, F., Rocchia, R., and Birck, J.-L., 2007, Osmium, tungsten, and chromium isotopes in sediments and in Ni-rich spinel at the K-T boundary: Signature of a chondritic impactor: Meteoritics & Planetary Science, v. 42, p. 1567–1580, https://doi.org/10.1111/j.1945-5100.2007.tb00591.x.

Rae, A.S.P., Collins, G.S.,, Morgan, J.V., et al., 2019, Impact-induced porosity and microfracturing at the Chicxulub impact structure: Journal of Geophysical Research–Planets, v. 124, no. 7, p. 1960–1978, https://doi.org/10.1029/2019JE005929.

Rasmussen, C., Stockli, D.F., Ross, C.H., Pickersgill, A., Gulick, S.P., Schmieder, M., Christeson, G.L., Wittmann, A., Kring, D.A., Morgan, J.V., and IODP-OCDP Expedition 364 Science Party, 2019, U-Pb memory

behavior in Chicxulub's peak ring—Applying U-Pb depth profiling to shocked zircon: Chemical Geology, v. 525, p. 356–367, https://doi.org/10.1016/j.chemgeo.2019.07.029.

Reimold, W.U., and Gibson, R.L., 2005, "Pseudotachylites" in large impact structures, *in* Koeberl, C., and Henkel, H., eds., Impact Tectonics, Impact Studies: Berlin, Springer, p. 1–53, https://doi.org/10.1007/3-540-27548-7_1.

Renne, P.R., Deino, A.L., Hilgen, F.J., Kuiper, K.F., Mark, D.F., Mitchell, W.S., III, Morgan, L.E., Mundil, R., and Smit, J., 2013, Time scales of critical events around the Cretaceous-Paleogene boundary: Science, v. 339, no. 6120, p. 684–687, https://doi.org/10.1126/science.1230492.

Riller, U., Poelchau, M.H., Rae, A.S., et al., 2018, Rock fluidization during peak-ring formation of large impact structures: Nature, v. 562, p. 511–518, https://doi.org/10.1038/s41586-018-0607-z.

Ross, C.H., Stockli, D.F., Rasmussen, C., Gulick, S.P.S., de Graaff, S.J., Claeys, P., Zhao, J., Xiao, L., Pickersgill, A.E., Schmieder, M., Kring, D.A., Wittmann, A., and Morgan, J., 2021, Evidence of Carboniferous Arc Magmatism Preserved in the Chicxulub Impact Structure: GSA Bulletin, https://doi.org/10.1130/B35831.1.

Schulte, P., Alegret, L., Arenillas, I., et al., 2010, The Chicxulub asteroid impact and mass extinction at the Cretaceous-Paleogene boundary: Science, v. 327, no. 5970, p. 1214–1218, https://doi.org/10.1126/science.1177265.

Schuraytz, B.C., Sharpton, V.L., and Marín, L.E., 1994, Petrology of impact-melt rocks at the Chicxulub multiring basin, Yucatán, Mexico: Geology, v. 22, no. 10, p. 868–872, https://doi.org/10.1130/0091-7613(1994)022<0868:POIMRA>2.3.CO;2.

Shukolyukov, A., and Lugmair, G.W., 1998, Isotopic evidence for the Cretaceous-Tertiary impactor and its type: Science, v. 282, no. 5390, p. 927–930, https://doi.org/10.1126/science.282.5390.927.

Sisson, T.W., and Grove, T.L., 1993, Temperatures and H_2O contents of low-MgO high-alumina basalts: Contributions to Mineralogy and Petrology, v. 113, p. 167–184, https://doi.org/10.1007/BF00283226.

Smit, J., 1999, The global stratigraphy of the Cretaceous-Tertiary boundary impact ejecta: Annual Review of Earth and Planetary Sciences, v. 27, p. 75–113, https://doi.org/10.1146/annurev.earth.27.1.75.

Smit, J., Montanari, A., Swinburne, N.H.M., Alvarez, W., Hildebrand, A.R., Margolis, S.V., Claeys, Ph., Lowrie, W., and Asaro, F., 1992, Tektite-bearing, deep-water clastic unit at the Cretaceous-Tertiary boundary in northeastern Mexico: Geology, v. 20, no. 2, p. 99–103, https://doi.org/10.1130/0091-7613(1992)020<0099:TBDWCU>2.3.CO;2.

Steiner, M.B., 2005, Pangean reconstruction of the Yucatán block: Its Permian, Triassic, and Jurassic geologic and tectonic history, *in* Anderson, T.H., Nourse, J.A., McKee, J.W., and Steiner, M.B., eds., The Mojave-Sonora Megashear Hypothesis: Development, Assessment, and Alternatives: Geological Society of America Special Paper 393, p. 457–480, https://doi.org/10.1130/0-8137-2393-0.457.

Stöffler, D., and Grieve, R.A.F., 2007, Impactites, *in* Fettes, D., and Desmons, J., eds., Metamorphic Rocks: A Classification and Glossary of Terms: Recommendations of the International Union of Geological Sciences: Cambridge, UK, Cambridge University Press, p. 82–92, 111–125, and 126–242.

Stöffler, D., Artemieva, N.A., Ivanov, B.A., Hecht, L., Kenkmann, T., Schmitt, R.T., Tagle, R.A., and Wittmann, A., 2004, Origin and emplacement of the impact formations at Chicxulub, Mexico, as revealed by the ICDP deep drilling at Yaxcopoil-1 and by numerical modeling: Meteoritics & Planetary Science, v. 39, no. 7, p. 1035–1067, https://doi.org/10.1111/j.1945-5100.2004.tb01128.x.

Sun, S.-S., and McDonough, W.F., 1989, Chemical and isotopic systematics of oceanic basalts: Implications for mantle composition and processes, *in* Saunders, A.D., and Norry, M.J., eds., Magmatism in the Ocean Basins: Geological Society [London] Special Publication 42, p. 313–345, https://doi.org/10.1144/GSL.SP.1989.042.01.19.

Swisher, C.C., Grajales-Nishimura, J.M., Montanari, A., et al., 1992, Coeval $^{40}Ar/^{39}Ar$ ages of 65.0 million years ago from Chicxulub crater melt rock and Cretaceous-Tertiary boundary tektites: Science, v. 257, no. 5072, p. 954–958, https://doi.org/10.1126/science.257.5072.954.

Taylor, S.R., and McLennan, S.M., 1981, The composition and evolution of the continental crust: Rare earth element evidence from sedimentary rocks: Philosophical Transactions of the Royal Society of London, ser. A, Mathematical and Physical Sciences, v. 301, no. 1461, p. 381–399, https://doi.org/10.1098/rsta.1981.0119.

Tuchscherer, M.G., Reimold, W.U., Koeberl, C., and Gibson, R.L., 2004a, Major and trace element characteristics of impactites from the Yaxcopoil-1 borehole, Chicxulub structure, Mexico: Meteoritics & Planetary Science, v. 39, no. 6, p. 955–978, https://doi.org/10.1111/j.1945-5100.2004.tb00939.x.

Tuchscherer, M.G., Reimold, W.U., Koeberl, C., Gibson, R.L., and de Bruin, D., 2004b, First petrographic results on impactites from the Yaxcopoil-1 borehole, Chicxulub structure, Mexico: Meteoritics & Planetary Science, v. 39, no. 6, p. 899–930, https://doi.org/10.1111/j.1945-5100.2004.tb00937.x.

Tuchscherer, M.G., Reimold, W.U., Koeberl, C., and Gibson, R.L., 2005, Geochemical and petrographic characteristics of impactites and Cretaceous target rocks from the Yaxcopoil-1 borehole, Chicxulub impact structure, Mexico: Implications for target composition: Meteoritics & Planetary Science, v. 40, no. 9–10, p. 1513–1536, https://doi.org/10.1111/j.1945-5100.2005.tb00415.x.

Tuchscherer, M.G., Reimold, W.U., Gibson, R.L., de Bruin, D., and Späth, A., 2006, Major and trace element compositions of melt particles and associated phases from the Yaxcopoil-1 drill core, Chicxulub impact structure, Mexico: Meteoritics & Planetary Science, v. 41, no. 9, p. 1361–1379, https://doi.org/10.1111/j.1945-5100.2006.tb00527.x.

Urrutia-Fucugauchi, J., Marin, L., and Trejo-Garcia, A., 1996, UNAM scientific drilling program of Chicxulub impact structure—Evidence for a 300 kilometer crater diameter: Geophysical Research Letters, v. 23, no. 13, p. 1565–1568, https://doi.org/10.1029/96GL01566.

van Westrenen, W., Blundy, J.D., and Wood, B.J., 2001, High field strength element/rare earth element fractionation during partial melting in the presence of garnet: Implications for identification of mantle heterogeneities: Geochemistry Geophysics Geosystems, v. 2, no. 7, 1039, https://doi.org/10.1029/2000GC000133.

Vermeesch, P.M., and Morgan, J.V., 2008, Structural uplift beneath the Chicxulub impact structure: Journal of Geophysical Research–Solid Earth, v. 113, no. B7, p. B07103, https://doi.org/10.1029/2007JB005393.

Ward, W.C., Keller, G., Stinnesbeck, W., and Adatte, T., 1995, Yucatán subsurface stratigraphy: Implications and constraints for the Chicxulub impact: Geology, v. 23, no. 10, p. 873–876, https://doi.org/10.1130/0091-7613(1995)023<0873:YNSSIA>2.3.CO;2.

Weber, B., Scherer, E.E., Martens, U.K., and Mezger, K., 2012, Where did the Lower Paleozoic rocks of Yucatán come from? A U-Pb, Lu-Hf, and Sm-Nd isotope study: Chemical Geology, v. 312–313, p. 1–17, https://doi.org/10.1016/j.chemgeo.2012.04.010.

Weber, B., González-Guzmán, R., Manjarrez-Juárez, R., de León, A.C., Martens, U., Solari, L., Hecht, L., and Valencia, V., 2018, Late Mesoproterozoic to early Paleozoic history of metamorphic basement from the southeastern Chiapas Massif complex, Mexico, and implications for the evolution of NW Gondwana: Lithos, v. 300–301, p. 177–199, https://doi.org/10.1016/j.lithos.2017.12.009.

Whitney, D.L., and Evans, B.W., 2010, Abbreviations for names of rock-forming minerals: The American Mineralogist, v. 95, no. 1, p. 185–187, https://doi.org/10.2138/am.2010.3371.

Wittmann, A., Kenkmann, T., Schmitt, R.T., Hecht, L., and Stöffler, D., 2004, Impact-related dike breccia lithologies in the ICDP drill core Yaxcopoil-1, Chicxulub impact structure, Mexico: Meteoritics & Planetary Science, v. 39, no. 6, p. 931–954, https://doi.org/10.1111/j.1945-5100.2004.tb00938.x.

Zhang, S.-Q., Mahoney, J.J., Mo, X.-X., Ghazi, A.M., Milani, L., Crawford, A.J., Guo, T.-Y., and Zhao, Z.-D., 2005, Evidence for a widespread Tethyan upper mantle with Indian Ocean–type isotopic characteristics: Journal of Petrology, v. 46, no. 4, p. 829–858, https://doi.org/10.1093/petrology/egi002.

Zhao, J., Xiao, L., Gulick, S.P.S., et al., 2020, Geochemistry, geochronology and petrogenesis of Maya block granitoids and dikes from the Chicxulub impact crater, Gulf of México: Implications for the assembly of Pangea: Gondwana Research, v. 82, p. 128–150, https://doi.org/10.1016/j.gr.2019.12.003.

Zürcher, L., and Kring, D.A., 2004, Hydrothermal alteration in the core of the Yaxcopoil-1 borehole, Chicxulub impact structure, Mexico: Meteoritics & Planetary Science, v. 39, no. 7, p. 1199–1221, https://doi.org/10.1111/j.1945-5100.2004.tb01137.x.